

Nature of the Galaxies On Top Of Quasars producing Mg II absorption

Labanya Kumar Guha,^{1*} Raghunathan Srianand^{1†}

¹*Inter-University Centre for Astronomy & Astrophysics, Pune, 411007, India*

Accepted XXX. Received YYY; in original form ZZZ

ABSTRACT

Quasar-galaxy pairs at small separations are important probes of gas flows in the disk-halo interface in galaxies. We study host galaxies of 198 Mg II absorbers at $0.39 \leq z_{abs} \leq 1.05$ that show detectable nebular emission lines in the SDSS spectra. We report measurements of impact parameter ($5.9 \leq D[kpc] \leq 16.9$) and absolute B-band magnitude ($-18.7 \leq M_B \leq -22.3$ mag) of host galaxies of 74 of these absorbers using multi-band images from the DESI Legacy Imaging Survey, more than doubling the number of known host galaxies with $D \leq 17$ kpc. This has allowed us to quantify the relationship between Mg II rest equivalent width (W_{2796}) and D , with best fit parameters of $W_{2796}(D=0) = 3.44 \pm 0.20 \text{ \AA}$ and an exponential scale length of $21.6^{+2.41}_{-1.97} \text{ kpc}$. We find a significant anti-correlation between M_B and D , and M_B and W_{2796} , consistent with the brighter galaxies producing stronger Mg II absorption. We use stacked images to detect average emissions from galaxies in the full sample. Using these images and stacked spectra, we derive the mean stellar mass ($9.4 \leq \log(M_*/M_\odot) \leq 9.8$), star formation rate ($2.3 \leq \text{SFR}[M_\odot \text{ yr}^{-1}] \leq 4.5$), age (2.5–4 Gyr), metallicity ($12 + \log(\text{O}/\text{H}) \sim 8.3$) and ionization parameter ($\log q[\text{cm s}^{-1}] \sim 7.7$) for these galaxies. The average M_* found is less than that of Mg II absorbers studied in the literature. The average SFR and metallicity inferred are consistent with that expected in the main sequence and the known stellar mass-metallicity relation, respectively. High spatial resolution follow-up spectroscopic and imaging observations of this sample are imperative for probing gas flows close to the star-forming regions of high- z galaxies.

Key words: galaxies: evolution; galaxies: high-redshift; galaxies: haloes; quasars: absorption lines

1 INTRODUCTION

Galaxies evolve through a slowly varying equilibrium between the gas inflows from the intergalactic medium (IGM), gas outflows from the galaxy to the circumgalactic medium (CGM) and the IGM, and insitu star-formation occurring within the galaxy (Erb 2008; Kennicutt & Evans 2012; Putman et al. 2012; Kacprzak 2017; Tumlinson et al. 2013). This is usually referred to as the “baryonic cycle”. Obtaining direct constraints on the gas inflow and outflow rates and how they evolve with redshift (i.e., cosmic time) is very important for our understanding of galaxy evolution.

Large-scale galactic outflows throw materials out to large distances and usually provide negative feedback to the ongoing star formation by preventing further gas accretion and/or not allowing the gas to cool down (Tumlinson et al. 2011). With time, however, the ejected material may cool and eventually fall back to the galactic disc to sustain subsequent star formation by giving rise to the so-called “galactic fountain” (Shapiro & Field 1976; Houck & Bregman 1990). In some cases, the wind may escape the galaxy and thereby enrich the IGM or the intra-group medium (for example, Samui et al.

2008). The signatures of galactic winds or the recycling of it are, more easily seen at the disk-halo interface, i.e., typically around a few kpc from the galactic disk.

The “down-the-barrel” spectroscopy of high- z galaxies, in principle, allows us to probe the connection between the properties of galaxies and the outflowing gas. Such studies confirm the ubiquitous presence of galactic scale outflows (with velocities of $100\text{--}1000 \text{ km s}^{-1}$), traced by the blue-shifted absorption lines of the neutral or singly ionized species like Na I, Mg II, Ca II and Fe II, in high redshift galaxies (e.g. Tremonti et al. 2007; Martin et al. 2012; Rubin et al. 2014; Bordoloi et al. 2014). However, it is difficult to constrain the exact locations of these outflows along our line of sight with respect to the galaxy and accurately measure the quantities like mass outflow rate. Spatially resolved galaxy spectra, either with the help of gravitationally lensed background sources (as in Lopez et al. 2018; Mortensen et al. 2021) or integral field spectroscopy aided with adaptive optics, will allow us to probe the spatial distribution of gas and its kinematics in more details.

Quasar absorption line studies, on the other hand, provide the physical conditions and the kinematics of the absorbing gas in the disk and/or the CGM of the foreground galaxy along a pencil beam. The Mg II $\lambda\lambda 2796, 2803$ absorption doublet present in the spectra of the background quasars is an excellent probe of cold ($T \sim 10^4 \text{ K}$) low-ionization gas associ-

* E-mail: labanya@iucaa.in (LG)

† E-mail: anand@iucaa.in (RS)

ated with a wide range of neutral hydrogen column densities (Srianand 1996; Rigby et al. 2002; Bond et al. 2001). Thanks to its rest wavelength, Mg II absorption from low- z galaxies (i.e., $0.3 \leq z \leq 1.0$) are easily accessible through ground-based optical spectroscopic observations. It is also well documented that the detection probability of DLAs and H I 21-cm absorption increases with increasing rest equivalent width of Mg II absorption (see for example, Rao et al. 2011; Gupta et al. 2012; Dutta et al. 2017a).

A quasar line of sight passing very close to the center of an intervening galaxy (within an impact parameter, $D \lesssim 15$ kpc) is bound to probe the disk-halo interface of the galaxy. Although efforts were made to study the Mg II absorption at small impact parameters (i.e., $D \lesssim 10$ kpc) for some galaxies (Kacprzak et al. 2013), they are all at low-redshift (i.e., $z < 0.1$). One way to find the quasar-galaxy pairs at such low impact parameters at high- z is to search for the host galaxies of Ultra-Strong Mg II absorption lines (USMgII, having rest equivalent width of Mg II $\lambda 2796$ line, $W_{2796} \geq 3\text{\AA}$) as they are expected to have extremely low impact parameters (D) based on the well known $W_{2796} - D$ anti-correlation (Chen et al. 2010; Nielsen et al. 2013a). However, it has been found in such absorbers that large equivalent widths not only originate from galaxies at low impact parameters but also from groups of galaxies (Nestor et al. 2011; Gauthier 2013; Guha et al. 2022).

Another efficient way of identifying quasar-galaxy pairs with low impact parameters is to search for nebular emission lines from the foreground galaxies in the SDSS fiber spectra of background quasars (Galaxies On Top Of Quasar – GOTOQ, as defined by York et al. 2012). In the case of GOTOQs, a star-forming foreground galaxy is present within an angular separation of $\sim 1''$ (SDSS DR-12) or $\sim 1.5''$ (SDSS DR-7) and the nebular line emissions from these foreground galaxies are present in the spectra of the background quasar.

Without any prior knowledge of the line of sight absorption, just by searching for nebular emission lines (like H α , [O III] and [O II]) from foreground galaxies in the SDSS quasar spectra, a total of 103 GOTOQ were identified in the redshift range $0 \leq z_{abs} \leq 0.84$ (Noterdaeme et al. 2010a; York et al. 2012; Straka et al. 2013; Straka et al. 2015). Using SDSS photometry, they detect galaxies in about 68% of the galaxies with impact parameters in the range of 0.37 to 12.68 kpc. As most of them are at $z < 0.3$, no information is available on the nature of Mg II absorption along the quasar sightlines. For GOTOQs at $z > 0.3$, Noterdaeme et al. (2010a) have shown that a strong Mg II absorption is always detected from the GOTOQs. Similarly, based on a very small sample of GOTOQs at $z < 0.1$ towards UV bright quasars, Kulkarni et al. (2022) have shown that nearly all of them are either DLAs or sub-DLAs.

The alternate approach to identifying the GOTOQs is to search for associated nebular emission lines (e.g., [O II]) in the quasar spectra at the known absorption redshift. Starting from the Mg II $\lambda\lambda 2796, 2803$ absorption doublet present on the background quasar spectra, if we search for associated [O II] $\lambda\lambda 3727, 3729$ emission which is ubiquitous in all star-forming galaxies, it will allow us to study the disk-halo interface of galaxies over the redshift range $0.35 \leq z \leq 1.5$. Joshi et al. (2018) have identified 198 GOTOQs associated with the Mg II absorbers (we provide more details in Section 2). The host galaxy properties (in terms of impact parameter

distribution, stellar mass, star formation rate, etc.) are not studied in detail till now. The availability of nearly uniform high-quality imaging data from the Dark Energy Spectroscopic Instrument (DESI) Legacy Imaging Survey (Dey et al. 2015, 2019) enables us to undertake such a study. This forms the main focus of this paper.

This paper is organized as follows. In section 2, we describe our sample and the corresponding spectroscopic and photometric data used in this work. In Section 3, we measure the properties of the individual host galaxies where it is possible to decompose the galaxy image from the quasar image. We also explore the correlations between the galaxy properties and properties of the absorption lines detected in the quasar spectra. In section 4, we use the stacked images and spectra to derive the average properties of the host galaxies of GOTOQs. Our findings on the nature of host galaxies of GOTOQs are summarised in section 5. For this work, we assume a flat Λ -CDM cosmology $H_0 = 70 \text{ km s}^{-1} \text{ Mpc}^{-1}$ and $\Omega_m = 0.3$.

2 SAMPLE & DATA

For this work, we consider the sample of GOTOQs associated with the known Mg II absorbers compiled by Joshi et al. (2017). In brief, Joshi et al. (2017) inspected all the quasar spectra showing intervening Mg II absorption (with $W_{2796} \geq 0.1\text{\AA}$) listed in the SDSS Fe II/Mg II metal absorber catalog of Zhu & Ménard (2013a) and searched for the associated [O II] $\lambda\lambda 3727, 3729$ nebular emission lines detected with more than 4σ significance. This has resulted in a total of 185 GOTOQs in the redshift interval $0.35 \leq z_{abs} \leq 1.05$. It is known that for a small fraction of high- z galaxies, the [O III] $\lambda\lambda 4960, 5008$ nebular emissions can be stronger than the [O II] $\lambda\lambda 3727, 3729$. To account for such galaxy populations, Joshi et al. (2017) searched for the [O III] emission doublets, detected with more than 3σ significance, associated with the Mg II absorption. This has resulted in 13 more GOTOQs based on [O III] emission for which the [O II] nebular emissions are detected at $< 4\sigma$ significance. Therefore, their sample contains a total of 198 GOTOQs. Among these GOTOQs, 67 were detected in SDSS-DR7 (that uses a fiber with a projected angular diameter of 3 arcsec), 117 were detected in SDSS-DR-12 (that uses a fiber with a projected angular diameter of 2 arcsec), and the rest of the 14 GOTOQs were observed both in SDSS-DR7 and SDSS-DR12.

Deep images of every quasar in this GOTOQ sample are available from the DESI Legacy Imaging Survey (Dey et al. 2015, 2019). We obtain images in all the available *grz* photometric bands. The DESI Legacy Imaging Survey is known to be complete up to an apparent *r* band magnitude of 23.6 mag. Assuming $M_r^* = -21.74$ mag (Karademir et al. 2022) and the *k*-correction to be negligible, this magnitude limit at the median redshift (i.e., $z_{abs} \sim 0.665$) of our GOTOQ sample corresponds to $\geq 0.12M_r^*$ galaxies. However, note that the detection sensitivity may not always reach this magnitude limit due to the presence of a bright quasar close to the foreground galaxy. We use the images from DESI Legacy Imaging Survey to study the nature of GOTOQs by direct decomposition of quasar and galaxy contributions and also using image stacking techniques. We also use all the SDSS spectra of quasars in the GOTOQ sample to investigate the

line of sight reddening, mean stellar and photospheric absorption, and nebular emission properties of the GOTOQs using spectral stacking techniques.

3 FOREGROUND GALAXY PROPERTIES

By construction, the quasar-galaxy pairs in the GOTOQ sample have exceptionally small impact parameters. Since the foreground galaxies are typically much fainter than the background quasars, they are either completely outshined by the background quasar or sometimes detected as an extension around the quasar in broadband photometry. Whether or not the foreground galaxy would be detected as a photometric extension to the quasar depends not only on the brightness of the background quasar and the foreground galaxy but also on the impact parameter and the orientation of the foreground galaxy with respect to the quasar sightline as well. Therefore, we individually inspected all the GOTOQ images from the DESI Legacy Imaging Survey and searched for the presence of photometric extensions around the background quasars beyond the point spread function (PSF).

3.1 Identifying the foreground galaxies

Purely based on the visual inspections of all the 198 GOTOQs in our sample, we have identified a total of 98 GOTOQs where another source is visible as a photometric extension around the background quasar. The method of identifying photometric extensions around the quasar based on visual inspections is illustrated in Figure 1. However, to make sure the identified photometric extensions are due to the foreground galaxies detected in emission on top of the quasar spectra and not due to chance coincidence of unrelated galaxies or stars, we consider only those cases for which the photometric redshift of the extensions are consistent within 2σ of the nebular emission redshifts. This brings down the total number of GOTOQs with the foreground galaxy detected as a broadband photometric extension to 84. The photometric redshifts of the sources associated with the photometric extensions are also obtained from the DESI Legacy Image Survey. The photometric redshifts are computed using the random forest algorithm. Details of the photo-z training and performance can be found in Zhou et al. (2021). They found a typical redshift uncertainty to be of the order 0.062 for objects with r-band magnitude brighter than the 23rd mag. The redshift uncertainty is larger than this for fainter sources.

Using the South African Large Telescope (SALT) spectroscopic follow-up of a [O II] line luminosity limited sub-sample consisting of 16 GOTOQs, we find that the photometric extensions with consistent photometric redshift are indeed due to foreground galaxies detected in emission in the quasar spectra (Guha et al., in preparation). Therefore, as in Straka et al. (2015), we consider the above-mentioned 84 galaxies to be foreground galaxies responsible for the [O II] emission and the Mg II absorption detected in the spectra of background quasars. From hereon, these sample GOTOQs for which the foreground galaxies are detected as broadband photometric extensions are referred to as ‘GOTOQ-Ext’.

Among these 84 GOTOQs, 25 were originally observed in SDSS-DR7, 56 were observed in SDSS-DR12, and the rest of the three were observed in both SDSS-DR7 and SDSS-DR12.

Table 1. Results of KS-test between the GOTOQ-Ext and GOTOQ-Noext sub-samples based on various photometric and spectroscopic properties.

Result	m_r	z_{abs}	$L_{[O II]}$	W_{2796}
p	0.023	0.059	0.125	0.198
D	0.219	0.193	0.171	0.156

For ten out of these 84 systems, the background quasars and the foreground galaxies are well separated in the sky plane, and the overlap between them is the bare minimum. Out of these ten GOTOQs, six are observed in SDSS-DR12, while the rest of the four are observed in SDSS-DR7. Given the typical SDSS seeing of $1.3''$, some fluxes from these galaxies may have leaked into the SDSS fiber used to observe the background quasar, thereby making these systems appear as GOTOQs. However, to be on the conservative side, we exclude them from our sub-sample of the GOTOQ-Ext as the true host galaxy may just sit on top of the quasar without producing any detectable photometric extensions. The details of these 84 systems with detected photometric extensions are listed in the Appendix in Table A1. The ten systems excluded are marked by an asterisk. Therefore, we have 74 systems in the sub-sample of ‘GOTOQ-Ext’.

For the remaining 114 GOTOQs (called the ‘GOTOQ-Noext’ sample), we do not find any significant photometric extensions around the quasar with consistent photometric redshifts. This fraction is much higher in our sample (i.e. $\sim 58\%$ compared to 31% found for the sample of Straka et al. 2015). The non-detection of any photometric extension in these 114 systems could stem either from one or the combination of the following reasons. The background quasars are relatively bright, the foreground galaxies are comparatively faint, and, the impact parameters are relatively small.

The Kolmogorov–Smirnov (KS) test between these two sub-samples (GOTOQ-Ext and GOTOQ-Noext) based on various properties are summarised in Table 1. The distributions are shown in Figure 2. The KS-tests yield p values of more than 0.05 for absorption redshift (z_{abs}), [O II] line luminosity, and the rest equivalent width of Mg II $\lambda 2796$ (W_{2796}) implying that the difference between these two sub-samples are statistically insignificant as far as these properties are concerned.

In the histogram plot of the r-band magnitude of the quasars, it is apparent that when the background quasars are relatively bright (low m_r), the fraction of GOTOQs having photometric extensions drops. Consequently, the KS-test yields a p value of 0.023. Other than the brightness of the background quasar, there are two additional factors (the brightness of the host galaxies and their impact parameters) that are important for the detection of the foreground galaxies as photometric extensions. In section 4, using the method of image stacking, we will explore the role of these two factors.

3.2 Individual measurements of impact parameters for the GOTOQ-Ext

We obtain the impact parameters of the host galaxies for the objects in the ‘GOTOQ-Ext’ sample using the decomposed locations of quasar and galaxy in the DESI Tractor

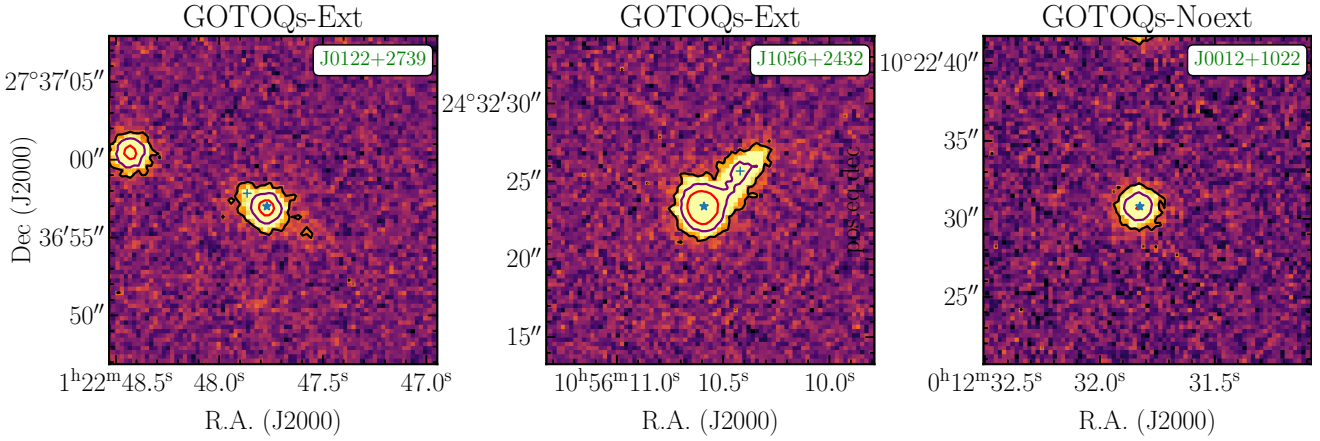


Figure 1. *Left and Middle panels:* Illustrations of GOTOQs showing the photometric extensions. The three panels show the DESI r-band images of three GOTOQ in our sample. *Right panel:* An example of quasar with a GOTOQ along the line of sight without showing any extension. For each panel, the quasar is marked with a blue ‘★’, and the contours correspond to the 3σ , 10σ , and 30σ levels above the mean background. The centroids of the photometric extensions are marked with a blue ‘+’. These were also identified as unique photometric source in the DESI Legacy Image Survey catalogs.

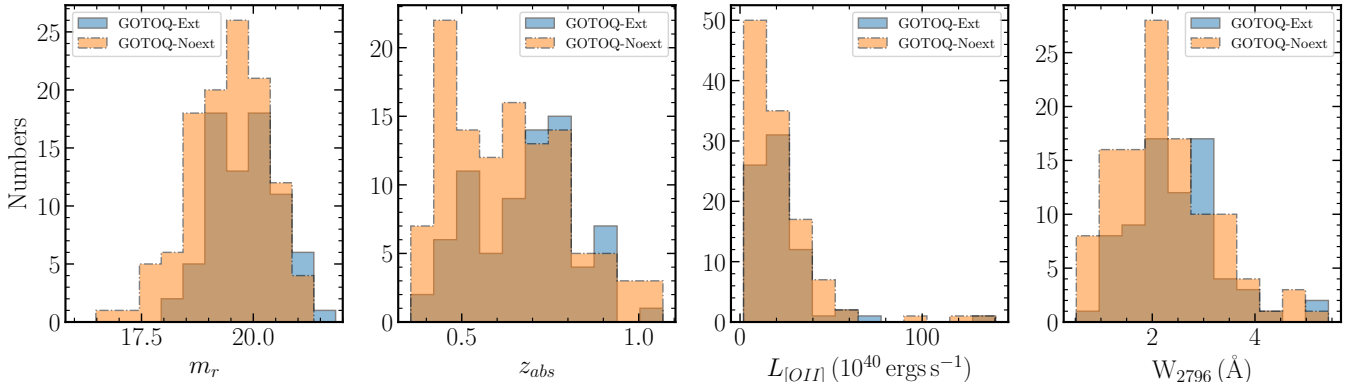


Figure 2. Comparison between systems with the photometric extensions (GOTOQ-Ext; blue histogram) and the systems without them (GOTOQ-Noext; orange histogram) based on various spectroscopic and photometric properties. From left to right, each panel shows the distributions of apparent r-band magnitude of the background quasar, Mg II absorption redshift, [O II] line luminosity, and W_{2796} .

Table 2. Results of Spearman Rank correlation.

Property 1	Property 2	r_S	p value
D	W_{2796}	-0.097	0.413
	W_{2852}	-0.074	0.546
	\mathcal{R}	-0.140	0.251
	$V_{\text{MgII-[OII]}}$	0.029	0.801
	z	0.282	0.015
	$L_{[\text{O II}]}$	0.157	0.182
	m_r^{qso}	-0.032	0.784
M_B	D	-0.464	3.123×10^{-5}
	z_{gal}	-0.183	0.118
	W_{2796}	-0.234	0.045

Catalog¹ (see section 8 of [Dey et al. 2019](#)). The projected physical separation between centroids of quasar and galaxy,

¹ <https://www.legacysurvey.org/dr9/description/#tractor-catalogs-1>

obtained for the cosmological parameters used in this work, is the impact parameter of the galaxy. In Figure 3, we compare the impact parameter distributions between objects in the ‘‘GOTOQ-Ext’’ sample with those identified based on the nebular emission line searches at relatively low redshifts ([Straka et al. 2015](#), hereafter refer to as S15 sample). In the case of the ‘‘GOTOQ-Ext’’ sample, we use the Mg II absorption redshift to be the redshift of the identified galaxy.

The red histogram in this figure corresponds to the impact parameter distribution of the S15 sample and the blue histogram corresponds to the same for objects in the ‘‘GOTOQ-Ext’’ sub-sample. The green and the orange histograms respectively show the impact parameter distributions of the objects in the ‘‘GOTOQ-Ext’’ sample observed in SDSS DR-7 and SDSS DR-12. The impact parameter of galaxies detected in S15 ranges from 0.37 kpc and 12.68 kpc with a median value of 4.83 kpc. Whereas the same in the case of our ‘‘GOTOQ-Ext’’ sample ranges from 5.9 kpc to 16.9 kpc with a median value of 10.85 kpc. From the impact parameter distributions, it is apparent that compared to our GOTOQ-Ext sample, the impact parameters of the objects in the S15 sample are smaller. A two-sample KS test yields an extremely low

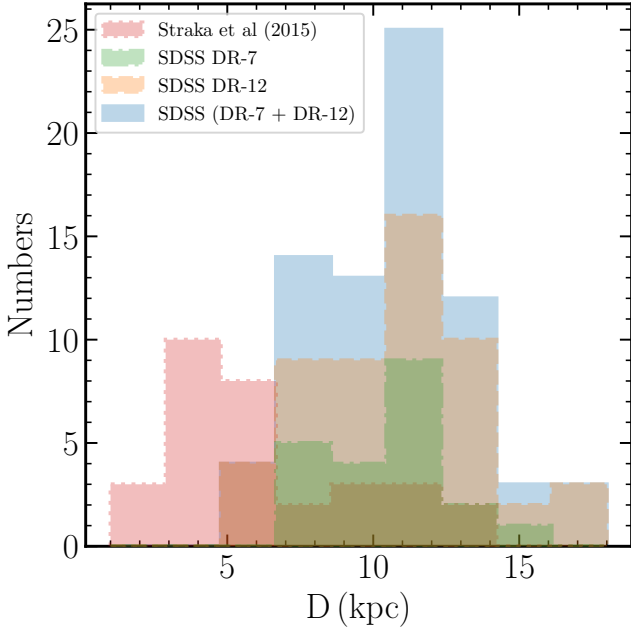


Figure 3. Comparison of the impact parameter distributions of low- z GOTOQs identified by [Straka et al. \(2015\)](#) (red histogram) with that of objects in our “GOTOQ-Ext” sample (blue histogram). The green and the orange histograms respectively show the impact parameter distributions of the objects in the “GOTOQ-Ext” sample observed in SDSS DR-7 and SDSS DR-12.

p -value of 8×10^{-11} , confirming that the impact parameter distributions for these two samples are very different.

This result is mainly due to selection bias. The S15 sample, which contains low-redshift galaxies, is biased against detecting galaxies at large impact parameters as the projected length scale for a fiber of a given radius will be lesser at these redshifts compared to redshifts of objects in our sample. It is also well documented that at a given redshift detection of nebular [O II] emission from GOTOQ is biased by the size of the fiber used. To see if the impact parameter distribution (that we obtain using the DESI Legacy Imaging Survey data) is biased by fiber size used in the spectroscopy to identify GOTOQs, we performed a two-sample KS test between the impact parameters of GOTOQs observed in SDSS-DR7 and SDSS-DR12. A high p -value of 0.42 obtained implies that the impact parameter distributions in our sample obtained here are not biased by the fiber size effects. Therefore, in what follows we do not treat GOTOQs detected from SDSS-DR7 and SDSS-DR12 differently when studying the galaxy properties.

Other than providing coordinates, the Tractor catalog also provides galaxy fluxes in different available photometric bands. We compute the apparent r -band magnitudes using the measured r -band fluxes and then convert this to the absolute rest frame B-band magnitude using the distance modulus of the absorbers and assuming the average SED fitted spectrum (see Section 4). The measured rest frame absolute B-band magnitude ranges from -22.32 to -18.72 mag. With $M_B^* = -21.53$ ([Faber et al. 2007](#)), this corresponds to a rest frame B-band luminosity range of $0.075L_B^*$ to $2.07L_B^*$.

3.3 Correlation between absorption properties and galaxy properties for the GOTOQ-Ext

In this section, we investigate possible correlations between the foreground galaxy properties (mainly impact parameter and B-band absolute magnitude, M_B) and properties derived using absorption lines in the case of “GOTOQ-Ext” sub-sample. Results of Spearman correlation are summarized in Table 2. The first two columns in this table list the properties compared and the last two columns give the correlation coefficient and p -value.

First, we examine the correlations between different parameters and the impact parameter. It is evident from the last column in Table 2 that there is no statistically significant correlation between the impact parameter and equivalent width of Mg II, Mg I, and Fe II to Mg II equivalent width ratio (i.e. \mathcal{R}). In particular, the lack of correlation between W_{2796} and D in our sample suggests a possible flattening in the well-known anti-correlation between these quantities at small D . This can be seen directly from the panel (d) of Figure 4. We discuss this in detail in section 3.4. The lack of any statistically significant difference in the W_{2796} distribution between the “GOTOQ-Ext” and “GOTOQ-Noext” sub-samples (Table 1 and Figure 2) are also consistent with the flattening of the distribution at low D .

We do not find any correlation between the velocity difference measured between Mg II absorption redshift and [O II] emission redshift (denoted by $V_{\text{MgII} - [\text{OII}]}$) and impact parameters. We do not also find any correlation between [O II] luminosity measured from the fiber spectra and impact parameter. Naively one expects the [O II] luminosity to be lower when the impact parameter is larger as more and more light will go through the fiber when D is small. However, this does not seem to strongly affect our sample.

Purely based on observational effects, we expect a possible anti-correlation between quasar magnitude and impact parameter. This is because when the quasar is bright, our ability to detect a galaxy at low impact parameters will be impaired. We do not see a statistically significant correlation even in this case. Only a marginally significant (p -value of 0.015) correlation is seen between z_{abs} and D . The impact parameters against the absorption redshifts for the “GOTOQ-Ext” sub-sample are plotted in the panel (c) of Figure 4. As discussed before, this could be related to the physical distance probed for a given angular scale being higher at higher redshifts.

Note, host galaxies of Mg II absorbers identified in the MAGICAT survey ([Nielsen et al. 2013b](#)) tend to show anti-correlation between impact parameter and absolute B-band magnitude ([Guha et al. 2022](#)). As can be seen from the panel (a) of Figure 4, there is a strong anti-correlation between the impact parameter and M_B with a correlation coefficient of -0.464 and a p -value of 3.123×10^{-5} in our sample as well. We also find, a possible anti-correlation (with a correlation coefficient of -0.234 and p -value of 0.045) between M_B and W_{2796} . This is also shown in panel (b) of Figure 4. This suggests that the brighter galaxies are typically associated with stronger Mg II absorption, albeit with a large scatter. If the absorbing galaxies in the “GOTOQ-Noext” sample are indeed faint, then the above-mentioned correlation may imply a statistically low W_{2796} for this sub-sample. However, as discussed above, the W_{2796} distributions for the two sub-

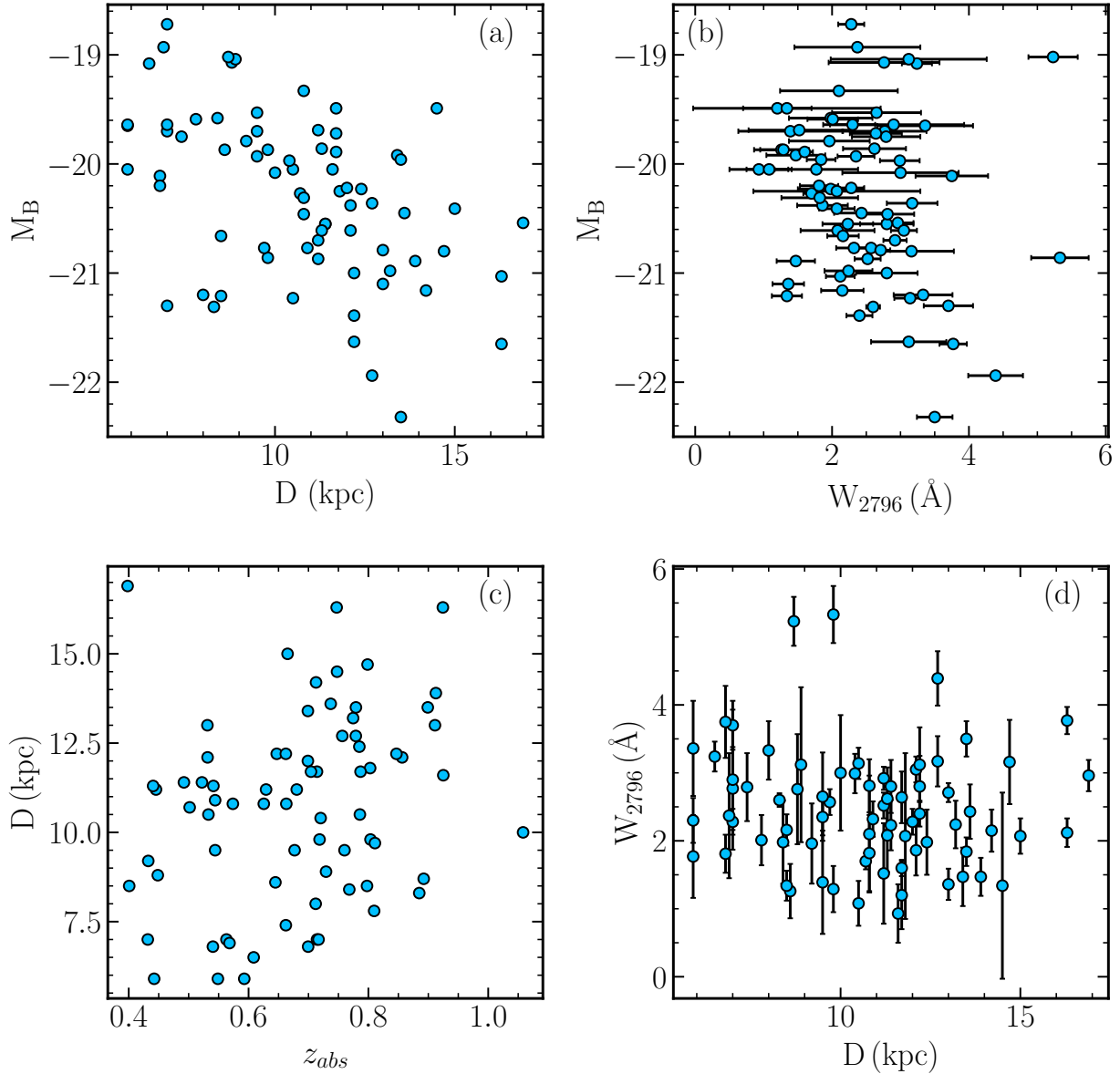


Figure 4. The plot showing significant correlations / anti-correlations found between different parameters in the sub-sample of “GOTOQ-Ext”. Panel (a) shows the absolute rest frame B-band magnitude of foreground galaxies versus the impact parameter. Panel (b) shows the absolute rest frame B-band magnitude of foreground galaxies versus the rest frame equivalent width of Mg II λ 2796 line. Panel (c) shows the impact parameters versus the absorption redshift, while Panel (d) shows W_{2796} against the impact parameter.

samples are statistically indistinguishable. This implies that the main reason for the non-detection of photometric extension in “GOTOQ-Noext” is related to the impact parameter being low and/or the background quasar being relatively bright. Below we address this in detail using stacked images.

In Figure 5, we plot the apparent (m_r in the left panel) and the rest frame B-band absolute (M_B in the right panel) magnitudes of galaxies against the absorption redshift. Even though there is a strong correlation seen between m_r and z , it is evident from this figure and Table 2 that there is no clear correlation between M_B with z_{abs} over the small redshift range considered here. The Spearman rank correlation coefficient is -0.183 with a p-value of 0.118 .

3.4 W_{2796} vs D correlation for galaxies in the GOTOQ-Ext sample

In the left panel of Figure 6, we plot the impact parameters obtained for objects in the “GOTOQ-Ext” sub-sample against W_{2796} . This plot also shows the same for the host galaxies of Mg II absorption systems studied in the literature (Kacprzak et al. 2013; Nielsen et al. 2013b; Dutta et al. 2020; Huang et al. 2021; Guha et al. 2022). As expected, our measurements have substantially increased the number of systems in the impact parameter range 5.9 to 16.9 kpc and provide stringent constraints on the W_{2796} distribution at low impact parameters. Excluding the “GOTOQ-Ext” sub-sample discussed here and the USMgII sample of Guha et al. (2022), only 35 Mg II host galaxies are identified in the liter-

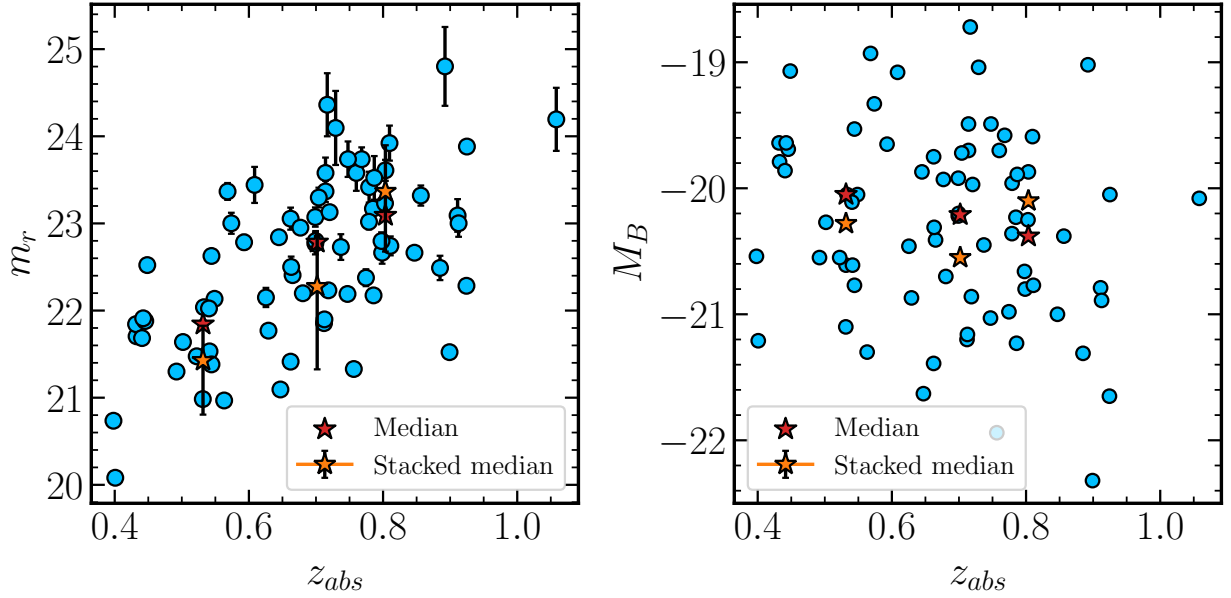


Figure 5. *Left panel* shows the r-band apparent magnitude of the foreground galaxies obtained from the DESI Legacy Survey Tractor catalog against the absorption redshifts. The red stars correspond to the median values of the apparent r-band magnitudes in the three redshift ranges considered here. The orange stars correspond to the measured r-band magnitudes in each of these bins obtained from the image stacking (see discussions in section 4). The error bar shown is the 16th to 84th percentile range obtained using bootstrapping. *Right panel* shows the same but for the rest frame B-band absolute magnitude calculated assuming the average SED spectrum.

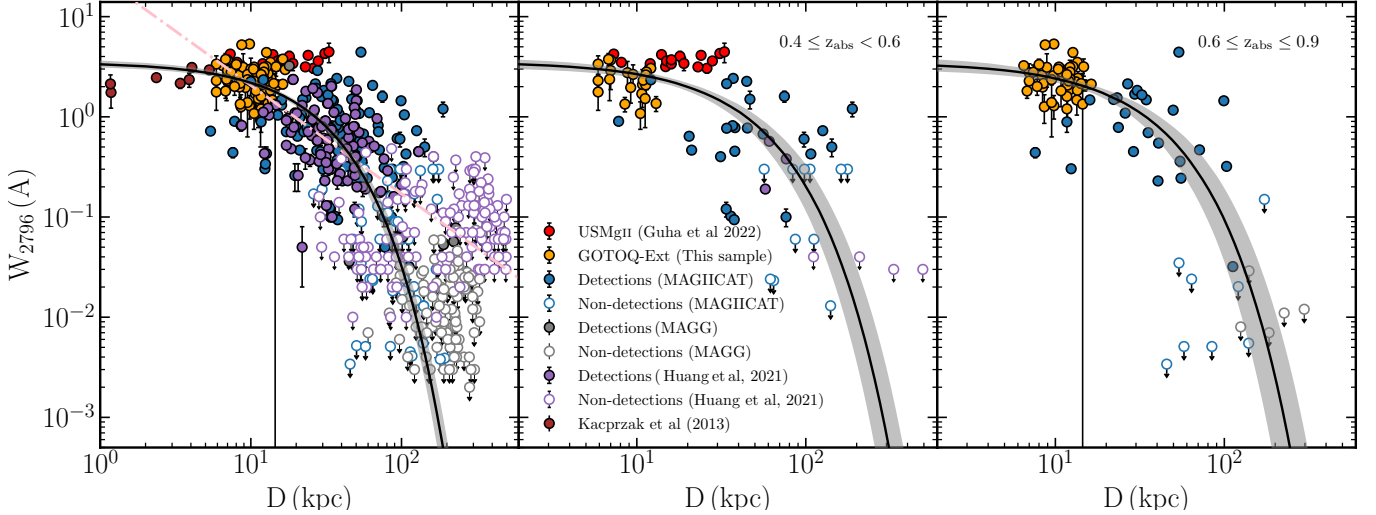


Figure 6. The *left panel* shows the impact parameter (D) versus the W_{2796} anti-correlation over the full redshift range for the isolated galaxies. Orange points are for the objects in the “GOTOQ-Ext” sub-sample. The red, blue, violet, gray, and brown points are taken from USMgII survey (Guha et al. 2022), MAGIICAT survey (Nielsen et al. 2013b), Huang et al. (2021), MAGG survey (Dutta et al. 2020), and Kacprzak et al. (2013) respectively. Note that in the MAGG survey, almost two-thirds of the Mg II absorption systems are associated with more than one galaxies (Dutta et al. 2020, 2021). We consider only the Mg II absorption systems associated with isolated galaxies. The solid black line corresponds to the best-fit log-linear model, and the shaded region corresponds to the 1σ errors associated with it. The GOTOQs typically follow the average anti-correlation. The *middle* and *right panel* show the same, but only for the redshift ranges, $0.4 \leq z_{abs} < 0.6$, and $0.6 \leq z_{abs} \leq 0.9$ respectively.

ature sample with $D \leq 17$ kpc over the entire redshift range. However, these systems are primarily from the low redshifts. There are only 10 and 4 systems present in the redshift range $0.4 \leq z_{abs} < 0.6$ and $0.6 \leq z_{abs} \leq 0.9$ respectively. The inclusion of 74 systems from the “GOTOQ-Ext” sub-sample substantially increases the total number of Mg II absorption systems in the low impact parameter ($D < 17$ kpc) range.

Our sample, therefore, is important in identifying the Mg II equivalent width at which the W_{2796} vs. D relationship flattens, the characteristic impact parameter, and their redshift evolution.

The solid black line in Figure 6 shows the maximum likelihood fit to the data assuming a log-linear function of the form $\log W_{2796} = \alpha D (\text{kpc}) + \beta$. To appropriately take into account

Table 3. The best fitted parameters for log-linear characterization of the $W_{2796} - D$ anti-correlation shown in Figure 6. Redshift ranges marked with * are for the fit without the USMgII systems.

Redshift	α	β	σ
0.09 - 1.49	-0.020 ± 0.002	0.537 ± 0.025	0.884 ± 0.036
0.09 - 1.49*	-0.022 ± 0.002	0.526 ± 0.028	0.792 ± 0.035
0.4 - 0.6	-0.012 ± 0.003	0.531 ± 0.046	1.090 ± 0.100
0.4 - 0.6*	-0.019 ± 0.005	0.514 ± 0.065	0.782 ± 0.091
0.6 - 0.9	-0.017 ± 0.004	0.547 ± 0.053	1.007 ± 0.098

the upper limits in the measurements of W_{2796} , we use the maximum likelihood method following the standard approach given in the literature (Chen et al. 2010; Rubin et al. 2014; Dutta et al. 2020; Guha et al. 2022). Note the above expression is identical to $W_{2796}(D) = W_{2796}(D=0) \exp(-D/h)$, with $W_{2796}(D=0) = 10^\beta$ and characteristic impact parameter scale $h = 1/(2.303 \times \alpha)$ kpc.

The best fit parameter for different sub-samples are summarized in Table 3. The gray region around the solid line in Figure 6 corresponds to 1σ uncertainty to the fit. For the full dataset (without any redshift cut) the best-fitted parameters obtained are $\alpha = -0.020 \pm 0.002$, $\beta = 0.537 \pm 0.025$ with an intrinsic scatter of $\sigma = 0.884 \pm 0.036$. This table also suggests that the exclusion of USMgII absorbers from the sample has very little effect on the derived parameters. The dot-dashed pink line corresponds to the power-law fit of the form $\log W_{2796} = \alpha \log D (\text{kpc}) + \beta$ with $\alpha = 24.9 \pm 3.1$, $\beta = 1.082 \pm 0.053$, and $\sigma = 0.979 \pm 0.043$. As indicated in previous studies, the power law fit overestimates the W_{2796} at low D and has a larger scatter at large D . Therefore, in what follows, we mainly use the log-linear fits.

Our best fit suggests that $W_{2796}(D=0) = 3.44 \pm 0.20 \text{ \AA}$ and $h = 21.6_{-1.97}^{+2.41}$ kpc. If we do not consider the GOTOQs from our sample, the best-fitted parameters are $\alpha = -0.019 \pm 0.002$, $\beta = 0.464 \pm 0.039$ with an intrinsic scatter of $\sigma = 0.914 \pm 0.042$ (Guha et al. 2022). This suggests that $W_{2796}(D=0) = 2.91 \pm 0.26 \text{ \AA}$ and $h = 22.85_{-2.17}^{+2.69}$ kpc. The value of $W_{2796}(D=0)$ we find here are higher than $1.87 \pm 0.47 \text{ \AA}$ found by Kacprzak et al. (2013) and $0.89_{-0.53}^{+1.45} \text{ \AA}$ by Dutta et al. (2020). It is evident from Figure 6 that three out of 7 of low- z points, that defined the $W_{2796}(D=0)$ in all previous studies, are below our fit by more than 3σ level. These differences noted could be related to either of (i) small number statistics at $D < 6$ kpc, (ii) redshift evolution (our data points are predominantly at $z > 0.36$ compared to $z \sim 0.1$ for the low- D data points from Kacprzak et al. (2013)) and (iii) intrinsic deviation from the smooth fit at low- D due to different feedback processes affecting the gas distribution. Therefore, it is important to increase the number of measurements at $D < 5$ kpc. In particular, identifying host galaxies in the case of the ‘‘GOTOQ-Noext’’ sub-sample using either space-based imaging or ground-based adaptive optics (AO) supported imaging may help in this regard.

Next, we investigate whether there is any redshift evolution in the W_{2796} vs D relationship by considering two sub-samples over the redshift range $0.4 \leq z_{abs} \leq 0.9$. In the middle and the left panels of Figure 6, we plot the same for the redshift ranges $0.4 \leq z_{abs} < 0.6$, and $0.6 \leq z_{abs} \leq 0.9$ respectively. Note in these redshift ranges our ‘‘GOTOQ-Ext’’ sub-sample contributes about 36% and 65% of the total sample. The fit

parameters are summarized in Table 3. It is clear from the table that the value of β (and hence $W_{2796}(D=0)$) and α (and hence h) are consistent between the two sub-samples. Thus, within the uncertainties in the derived parameters, we do not see any statistically significant redshift evolution. It is also evident from the table that this result does not change even when we do not consider the data points for USMgII sample for $0.4 \leq z_{abs} < 0.6$. Lack of redshift evolution in the W_{2796} vs. D relationship was already discussed in the literature (see for example, section 3.6 of Dutta et al. 2020).

4 RESULTS FROM THE STACKING ANALYSIS

As we discussed before, we do not have a clear identification of host galaxies of GOTOQs in 58% of the cases. Here, we use image and spectral stacking techniques to draw some inferences on the nature of the host galaxies of these GOTOQs.

4.1 Stacking of quasar images

We obtained the multiband (g , r , and z bands) deep photometric images of all the 198 GOTOQs from the DESI legacy imaging Survey. For each GOTOQ, we have downloaded a 256×256 pixels cutout of the image centered around the quasars. These are flux-calibrated and continuum-subtracted images. The width of each pixel in these images corresponds to the angular scale of 0.27 arcsec. Before we perform the image stacking, we mask all the unrelated sources (in particular galaxies at low impact parameters having inconsistent photometric redshifts) present in the field so that the rms of the background counts in the final stacked image can be estimated accurately. We used the iterative σ -clipping method to estimate the mean (nearly zero) and the standard deviation (σ_{bkg}) of the background for every image and masked all the pixel having values more than $3\sigma_{bkg}$ above the mean background and replace them with the mean background values. Once the masking of all the GOTOQ fields is performed, we visually inspected them to ensure that we have masked all the other sources except for the GOTOQs and the associated photometric extensions in the case of objects in the GOTOQ-Ext sub-sample. We then performed a simple median stacking of images separately for each of the above-mentioned three photometric bands.

To estimate the average fluxes of the foreground galaxies in different bands we need to subtract the contributions of the quasar and its host galaxy from the stacked image. This we do by using the stacked images of an appropriately chosen control sample of quasars. We used quasars in the SDSS sample to construct the control sample. For every quasar in our GOTOQ sample, we randomly identified 5 quasars satisfying the following criteria: (i) Similar emission redshifts, i.e., $|\Delta z| \leq 0.005$; (ii) Similar SDSS r -band apparent magnitude, i.e., $|\Delta m_r| \leq 0.25$ mag and (iii) No Mg II absorption (having $W_{2796} \geq 0.5 \text{ \AA}$) detected in the quasar spectra with at least 3σ significance. Except for five cases, where we could not find five quasars satisfying all three conditions, we slightly relaxed the first two conditions to find a total of five quasars with similar redshifts and apparent magnitudes and without any Mg II absorption present along the line of sight. Therefore, corresponding to 198 GOTOQs in our sample, there are a total of 990 quasars in our control sample.

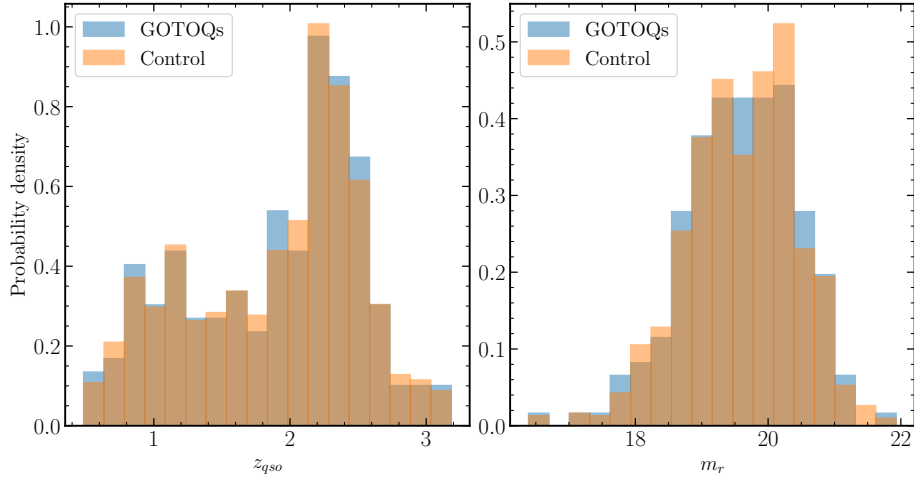


Figure 7. Comparison of the distributions of emission redshift (left panel) and r-band magnitude (right panel) of quasars in the GOTOQ sample (blue) and in the control sample (orange). As designed, these distributions are consistent with being drawn from the same parent population.

In Figure 7, we compare the redshift and the apparent magnitude distributions of quasars in our GOTOQ sample and in the control sample. The KS-test between the redshift and m_r distributions of the GOTOQs and the control sample yields p values of 1.00 and 0.92 respectively. This reconfirms that both samples are drawn from the same parent population as far as these two properties are concerned. The g , r , and z band images of these 990 quasars were also obtained from the DESI legacy survey. As in the case of GOTOQs, we first masked all the other sources present in the image and performed the stacking to obtain the median stacked images of the control sample in all three different bands.

4.1.1 Host galaxy luminosity and impact parameter

The GOTOQs in our sample spread over a wide redshift range. For the lowest redshift GOTOQ ($z_{abs} = 0.3662$), one pixel in the image corresponds to a physical scale of 1.37 kpc while that for the highest redshift ($z_{abs} = 1.0582$) GOTOQ is 2.19 kpc. To minimize the effect of angular to physical scale dependence on redshift, we sub-divide our sample into three redshift bins (with an equal number of objects for the GOTOQ-Ext sample in each bin) and performed the image stacking of GOTOQs and the corresponding control sample QSOs.

In the top panel of Figure 8, we show the r-band stacked images of the GOTOQs in three redshift bins after subtracting the corresponding images of the control sample. We clearly detect significant emissions from galaxies in all three redshift bins. The green contours in these panels show the $3\sigma_{bkg}$ level of the background noise. In the bottom panel of Figure 8, we show the radially averaged flux profiles as a function of radial distance. Green dotted lines give the $3\sigma_{bkg}$ value of the background. The error bars show the 16th to 84th percentiles range of the measured data points obtained with bootstrapping by removing and replacing 20% of the quasars from the given sample with 100 realizations. The vertical gray line provides the radial distance up to which galaxy emission is detected above $3\sigma_{bkg}$ level (the same is shown as dark circles in upper panels on the angular scale). This radial profile,

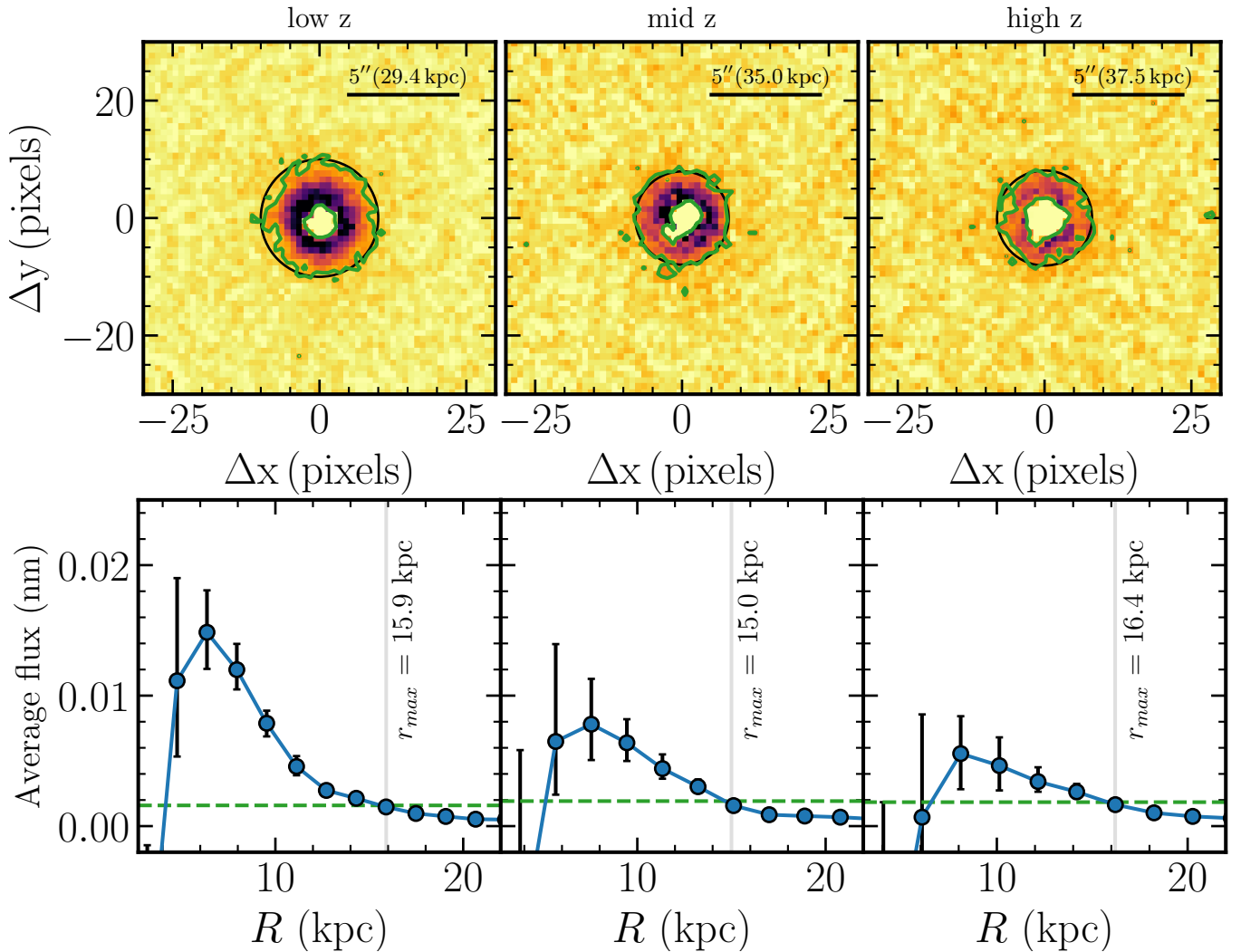
which we measure from the stacked spectrum, is influenced by the intrinsic light profile of individual galaxies, the impact parameter distribution of galaxies, and the point spread function (PSF) of the observations. Therefore, the maximum distance up to which we can detect galaxy light provides a conservative upper limit on the impact parameter. The maximum impact parameters for the three redshift bins range from 15.0 kpc to 16.4 kpc. These are consistent with our expectations based on the projected size of fibers used in the SDSS spectroscopy and what we measure in the case of individual objects in the "GOTOQ-Ext" sub-sample.

In all figures, we notice a reduction in the flux close to the center. Whether this reduction is due to the over-subtraction or lack of galaxies close to the impact parameter zero, we perform the following exercise. For each quasar in our GOTOQ sample, out of the available five quasars in the control sample, we randomly select four quasars. Next, we constructed two different control sub-samples (designated as 'A' and 'B') with the first two quasars in the control sub-sample 'A' and the other two in the control sub-sample 'B'. Then, we create the median stacks for these two control sub-samples and subtract one from the other. The obtained residual is more or less consistent with zero and without any significant circular regions with negative counts in the center. Thus, the 'hole' present in the stacks of GOTOQs is most likely to be related to the lack of galaxies close to zero impact parameters. Note presence of such GOTOQs would have considerably reddened the quasar, and probably the color selection used in SDSS would have missed such highly reddened objects. We integrate the flux in all the pixels of the residual image where the detection is above the $3\sigma_{bgr}$ level (i.e., between the inner and outer green contours). These are summarized in Table 4. We used this to obtain the average apparent magnitudes in the three bands used here and the absolute magnitude in the B-band (M_B , assuming the average galaxy SED discussed below). The median M_B obtained in these three redshift bins corresponds to a $\sim 0.3L_*$ galaxy (Faber et al. 2007) at these redshifts.

Next, we perform the image stacking of objects in the "GOTOQ-Ext" and "GOTOQ-Noext" sub-samples in the same three redshift bins. The resulting residual images are

Table 4. Estimated average galaxy properties based on the photometric and spectroscopic stacking. The values in the parenthesis correspond to the 1σ uncertainty. Line luminosities are measured in the units of 10^{40} ergs s^{-1} .

Redshift	Sample	m_g	m_r	m_z	$L_{[O\ II]}\lambda 3728$	$L_{H\beta}\lambda 4862$	$L_{[O\ III]}\lambda 4960$	$L_{[O\ III]}\lambda 5008$
0.35 - 0.625 (low- z)	All	$22.97^{+0.56}_{-0.89}$	$21.80^{+0.23}_{-0.26}$	$22.16^{+0.48}_{-0.65}$	9.98(0.32)	3.48(0.25)	2.57(0.27)	6.93(0.25)
	GOTOQ-Ext	$22.63^{+0.85}_{-0.95}$	$21.43^{+0.40}_{-0.68}$	$21.04^{+0.26}_{-0.37}$	11.2(0.5)	4.0(0.4)	2.9(0.4)	11.0(0.5)
	GOTOQ-Noext	$22.90^{+0.65}_{-0.97}$	$22.32^{+0.31}_{-0.82}$	$22.11^{+0.39}_{-0.71}$	9.7(0.4)	2.96(0.31)	2.75(0.31)	5.70(0.31)
0.625 - 0.748 (mid- z)	All	$23.39^{+0.59}_{-0.85}$	$22.37^{+0.35}_{-0.58}$	$22.89^{+0.44}_{-0.93}$	18.9(0.7)	3.8(0.6)	4.2(0.9)	10.9(0.8)
	GOTOQ-Ext	$22.38^{+0.73}_{-1.03}$	$22.27^{+0.58}_{-0.95}$	$22.81^{+0.53}_{-0.83}$	19.8(0.8)	4.3(0.9)	5.7(1.2)	11.9(1.2)
	GOTOQ-Noext	$22.63^{+0.97}_{-0.60}$	$22.34^{+0.62}_{-0.68}$	$22.49^{+0.70}_{-0.70}$	19.7(1.0)	≤ 2.7	4.3(1.3)	10.6(1.4)
0.748 - 1.06 (high- z)	All	$24.00^{+0.59}_{-1.10}$	$22.78^{+0.51}_{-0.70}$	$23.07^{+0.52}_{-1.12}$	25.5(0.8)	9.5(1.3)	≤ 7.2	22.4(2.4)

**Figure 8.** *Top panel:* The r -band stacked images of the GOTOQs in three redshift bins after subtracting the contributions from the QSO and its host galaxy using the control sample of quasars. The $3\sigma_{bgr}$ contours are shown in green. From the left to the right, the three panels correspond to the low- z , mid- z , and high- z bins (see Table 4) respectively. *Bottom panel:* The radially averaged flux profiles (in nanomaggy) of the images shown in the top panel as a function of radial distance. The shown errors are obtained using bootstrapping. The green dashed horizontal line corresponds to the $3\sigma_{bgr}$. The solid gray vertical line shows the radial distance where the flux falls below the $3\sigma_{bgr}$. The black circles in the top panel indicate the radius (in the angular scale) corresponding to the r_{max} .

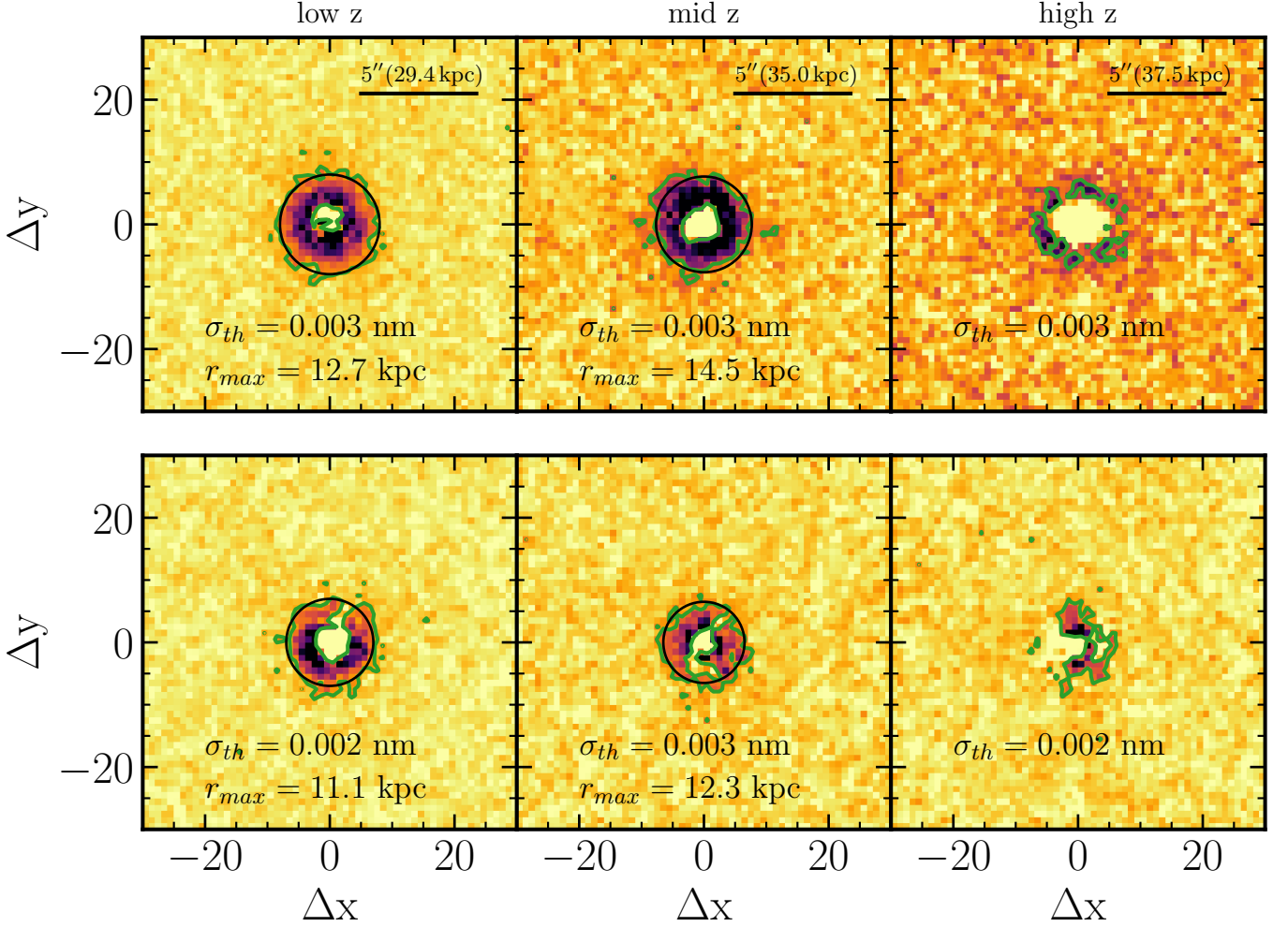


Figure 9. Residual r-band fluxes for the three redshift bins. The top and bottom panels correspond to the “GOTOQ-Ext” and “GOTOQ-Noext” sub-samples. The black circle corresponds to the radius of r_{max} beyond which the average residual flux falls below the σ_{th} (i.e. $3 \times \sigma_{bgr}$). In each panel we provide σ_{th} (in nanomaggy) and r_{max} .

shown in Figure 9. In the top panel, we show the results for the “GOTOQ-Ext” sample for the three redshift bins in the r-band. The absorbing galaxies are clearly detected in the low- z and mid- z bins. The detection is marginal for the high- z bin. The measured apparent magnitudes in different bands and M_B are also summarized in Table 4. Next, we compare the mean magnitude (m_r and M_B) obtained from the stacking (yellow star) with that from the individual measurements (red star) obtained for “GOTOQ-Ext” (see Figure 4). For the low- z and mid- z bins, the estimated r-band magnitudes from the stacked images are up to 0.5 mag brighter than the median magnitudes from the direct measurements for the “GOTOQ-Ext” sub-sample. However, in the high- z bin they are consistent with one another. The excess seen for the low- z and mid- z bins could be related to a possible over-subtraction of QSO+host galaxy contribution in individual images due to larger σ_{bgr} compared to that in our stacked images. High spatial resolution images are needed to understand the origin of this difference. If Figure 9, we also indicate the maximum impact parameters. While these values are consistent with direct measurements, they are slightly

lower than what we find for the full sample (see Figure 8). This is mainly because of the increase in the σ_{bgr} in the case of the “GOTOQ-Ext” sub-sample.

In the bottom panel of Figure 9, we show the results for the “GOTOQ-Noext” sub-samples. We detect the host galaxies at a highly significant level in both low- z and mid- z bins. As there are more objects in this sub-sample compared to “GOTOQ-Ext” sub-sample the σ_{bgr} are slightly better for the “GOTOQ-Noext” sub-sample. Despite this, we measure the r_{max} to be smaller than what we have found for “GOTOQ-Ext” sub-sample. Also, as can be seen from Table 4 in the r-band (where we have the best SNR), the measured absolute magnitude in the case of “GOTOQ-Noext” is less than that of “GOTOQ-Ext” sub-sample. Based on this, we can infer that the non-detection of extended features in “GOTOQ-Noext” is due to the impact parameters being smaller and the galaxies being fainter in this sub-sample.

4.2 Stacking of quasar spectra

In this section, we focus on the average galaxy spectrum obtained after removing the quasar contribution with the help of spectral stacking. We use this and the stacked images to derive the average properties of the host galaxies of the GOTOQs. We adopt the following procedure for the spectral stacking exercise. We first scale every quasar spectrum by an appropriate factor so that the flux in the individual spectrum matches well with a reference r-band flux. Next, to avoid contamination from the Ly α forest absorption, we consider the wavelength range of the quasar spectrum that satisfies,

$$\lambda_{obs} \geq (1 + z_{qso}) \times 1216 \text{ \AA} \times \left(1 + \frac{10^4 \text{ km s}^{-1}}{c}\right)$$

with ‘c’ being the speed of light. Doppler shift corresponding to 10000 km s^{-1} is applied to avoid the N v emission line and possible associated absorption lines. Finally, we deredshift every quasar spectrum to the rest-frame wavelength of the Mg II absorption by keeping the total flux conserved and re-sample the spectra to a common wavelength axis with $\Delta\lambda = 1 \text{ \AA}$. As the rest wavelength range of individual quasar spectrum varies depending on the Mg II absorption redshift, not all quasars contribute to a given rest wavelength in the stacked spectrum. However, we note that almost all quasars in the GOTOQ sample contribute to the stacking over the rest wavelength range 2800-5000 Å.

4.2.1 Rest equivalent widths of absorption lines and dust extinction

First, we study the rest equivalent widths of different absorption lines present in the stacked spectrum. For this, we consider the geometric mean of the continuum normalized spectra. We first exclude the wavelength range affected by the emission and absorption line features for the continuum normalization and use PYQSOFIT (Guo et al. 2018) to fit the quasar continuum. The rest equivalent widths of different absorption lines detected in the stacked spectra for the full and different sub-samples are summarized in Table 5. We also compare these with the results obtained from the stacked spectra of strong Mg II absorbers (i.e., $W_{2796} > 2.0$) by York et al. (2006, Y06), Ca II absorbers by Sardane et al. (2015, S15) and H I 21-cm absorbers by Dutta et al. (2017a, D17). We chose these data sets as strong Mg II absorbers (based on W_{2796} vs. D anti-correlation), Ca II absorbers (Wild et al. 2007, who found stronger [O II] emission in the composite spectra of Ca II absorbers compared to Mg II absorbers) and H I 21-cm absorbers (Gupta et al. 2010; Dutta et al. 2017b) tend to probe galaxies at smaller impact parameters as in GOTOQs.

The average rest equivalent widths of Mg II measured in our sample is much higher than that measured for the Ca II-selected and H I 21-cm absorbers. This is also the case for strong Fe II transitions (at rest wavelengths 2344, 2374, 2383, 2586, and 2600 Å). While the composite spectrum of Y06 (of systems with $W_{2976} \geq 2 \text{ \AA}$) has similar Mg II equivalent widths, all the other strong transitions have equivalent widths lower than what we measure for GOTOQs. This could imply a large spread in line-of-sight velocity (or the number of individual absorption components) in the case of GOTOQs compared to other populations of absorbers considered here. The rest equivalent widths of the strongest transitions of Mg II and

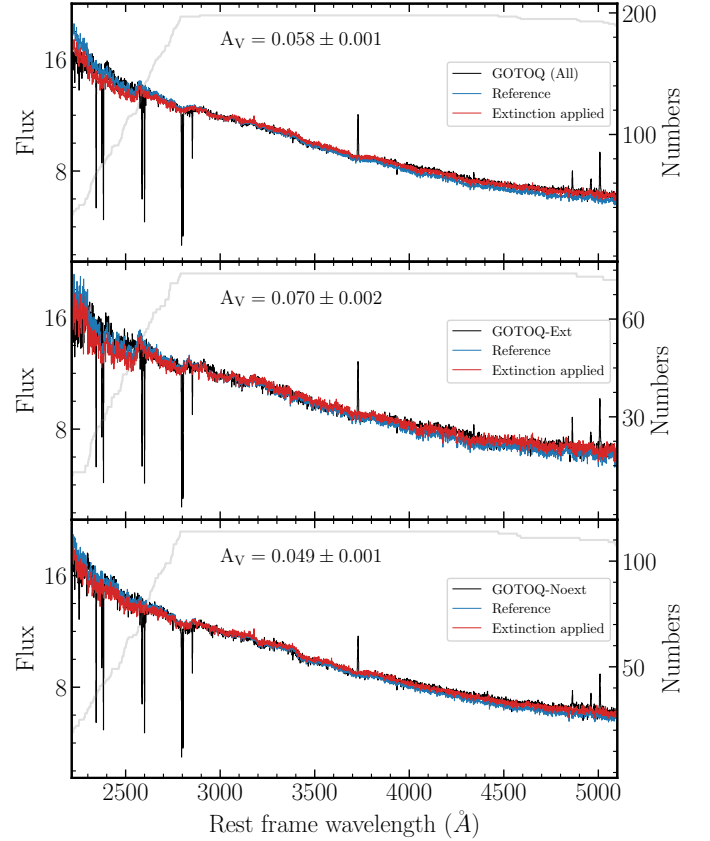


Figure 10. Average reddening of the background quasars by all the GOTOQ in our full sample (top panel), “GOTOQ-Ext” (middle panel) and “GOTOQ-Noext” (bottom panel). The black spectrum in each panel is the geometric mean composite of the appropriate GOTOQ sample, the corresponding reference spectrum is shown in the blue and red spectrum corresponds to the best-fit reddened reference spectrum using the SMC extinction curve. The best-fitted A_V values are indicated in each panel. The gray line gives to the number of quasars contributing to the stack at a given wavelength.

Fe II, which are expected to be highly saturated, are higher for the “GOTOQ-Ext” sub-sample compared to that of the “GOTOQ-Noext” sub-sample.

Interestingly the Mn II equivalent widths we find for the GOTOQs are consistent with what has been measured for H I 21-cm absorbers and slightly larger (albeit within error) in the case of Ca II selected absorbers. Unlike the singly ionized species of Mg and Fe, Mg I equivalent width is nearly identical among different sub-sample. Dutta et al. (2017a) have shown that, for the similar Mg II equivalent widths, the absorbers showing H I 21-cm absorption (i.e. DLAs with cold neutral gas) tend to show detectable Mn II in the SDSS spectra. All this implies most of the GOTOQs will be DLAs (As confirmed for $z < 0.15$ by Kulkarni et al. 2022) specifically having larger velocity spread in singly ionized species compared to systems selected based on other tracers.

The Ca II absorption lines are clearly detected in our stacked spectrum. The measured equivalent width for the full GOTOQ sample is slightly higher than what is measured in the case of the strong Mg II absorber of Y06 but much weaker than what is found for Ca II-selected absorbers of S15. Among different sub-sample discussed by York et al.

Table 5. Rest equivalent widths of the spectroscopic transitions detected in the geometric mean stacked quasar spectrum of the GOTOQ.

Transition	Rest equivalent width (Å)					
	All	GOTOQ-Ext	GOTOQ-Noext	Y06	S15	D17
Fe II λ 2249	≤ 0.10	≤ 0.18	≤ 0.21	0.11 ± 0.01	0.126 ± 0.012	0.15 ± 0.04
Fe II λ 2260	0.10 ± 0.03	≤ 0.20	≤ 0.20	0.11 ± 0.01	0.115 ± 0.011	0.13 ± 0.04
Fe II λ 2344	1.69 ± 0.08	1.76 ± 0.13	1.63 ± 0.10	1.20 ± 0.01	1.140 ± 0.009	1.06 ± 0.04
Fe II λ 2374	1.16 ± 0.08	1.27 ± 0.11	1.06 ± 0.06	0.70 ± 0.01	0.751 ± 0.009	0.85 ± 0.07
Fe II λ 2382	2.03 ± 0.03	2.03 ± 0.10	2.03 ± 0.11	1.60 ± 0.01	1.398 ± 0.009	1.69 ± 0.07
Fe II λ 2586	1.49 ± 0.07	1.57 ± 0.06	1.40 ± 0.06	1.14 ± 0.01	1.115 ± 0.008	1.23 ± 0.06
Fe II λ 2600	1.84 ± 0.06	1.94 ± 0.09	1.71 ± 0.07	1.67 ± 0.01	1.472 ± 0.008	1.68 ± 0.06
Mn II λ 2576	0.26 ± 0.04	0.36 ± 0.10	0.22 ± 0.06	0.14 ± 0.01	0.226 ± 0.010	0.28 ± 0.06
Mn II λ 2594	0.25 ± 0.04	0.30 ± 0.06	0.27 ± 0.05	0.13 ± 0.01	0.164 ± 0.009	0.20 ± 0.06
Mn II λ 2606	0.13 ± 0.04	≤ 0.21	≤ 0.15	0.08 ± 0.01	0.104 ± 0.009	0.14 ± 0.06
Mg II λ 2796	2.52 ± 0.03	2.66 ± 0.05	2.44 ± 0.06	2.67 ± 0.01	1.940 ± 0.008	2.22 ± 0.08
Mg II λ 2803	2.29 ± 0.04	2.45 ± 0.04	2.16 ± 0.07	2.40 ± 0.01	1.803 ± 0.008	2.08 ± 0.07
Mg I λ 2852	0.73 ± 0.02	0.67 ± 0.03	0.72 ± 0.05	0.59 ± 0.01	0.742 ± 0.007	0.77 ± 0.07
Ti II λ 3384	0.17 ± 0.06	0.15 ± 0.05	≤ 0.17	0.082 ± 0.007
Ca II λ 3934	0.34 ± 0.06	0.29 ± 0.05	0.37 ± 0.08	0.703 ± 0.006
Ca II λ 3969	0.15 ± 0.05	≤ 0.15	0.17 ± 0.05	0.418 ± 0.006

(2006) only the sub-sample of absorbers showing detectable Zn II absorption have shown Ca II equivalent width close to what we find in our GOTOQ sample. [Zhu & Ménard \(2013b\)](#) have found a relationship between Ca II rest equivalent in the stacked spectrum with impact parameter using SDSS QSO-Galaxy pairs (at $z \sim 0.1$) up to a projected distance of 200 kpc. For the impact parameter bin 3-10 kpc (with a median of 7 kpc) they found the rest equivalent width of Ca II λ 3934 to be $0.435 \pm 0.068 \text{ \AA}$. However, as in the case of Mg II discussed above a flattening in the $W(\text{Ca II})$ vs. D relationship is noticed when individual measurements at $D < 15$ kpc are considered ([Straka et al. 2015](#); [Rubin et al. 2022](#)). The fit by [Rubin et al. \(2022\)](#) predicts the $W(\text{Ca II})$ in the range $0.36\text{--}0.48 \text{ \AA}$ for $D < 14$ kpc. The Ca II rest equivalent width we measure (i.e. $0.34 \pm 0.06 \text{ \AA}$) in our stacked spectrum is consistent with the above measurements at low redshifts. Another interesting thing we notice is that $W(\text{Ca II})$ obtained for the “GOTOQ-Noext” sub-sample is slightly higher than that of the “GOTOQ-Ext” sub-sample.

Next, we measure the average dust extinction using the geometric mean composite of the GOTOQ spectra as it is better suited to study the absorption properties. Using the composite spectrum of the control sample as a reference, we apply the SMC dust extinction law ([Gordon et al. 2003](#)) and vary the V-band extinction coefficient, A_V to match the continuum of the composite spectrum of the GOTOQ. Our method is similar to what is described in [Srianand et al. \(2008\)](#); [Guha et al. \(2022\)](#). The composite spectrum of the full GOTOQ sample, corresponding control sample and the best fit spectrum after applying extinction is shown in the top panel of Figure 10. This resulted in the best fit value of $A_V = 0.058 \pm 0.001$ that corresponds to the color excess of $E(B - V) = 0.021 \pm 0.001$. This is consistent with what is found for the full Ca II-selected absorbers (see [Sardane et al. 2015](#)) but less than what is found for the strong Ca II-selected absorbers and H I 21-cm absorbers ([Dutta et al. 2017a](#)). The color excess we measure for GOTOQs is consistent with strong ($2 \text{ \AA} \leq W_{2796} \leq 6 \text{ \AA}$) Mg II absorbers with high values ($\mathcal{R} \geq 0.5$) of $W_{2600}^{\text{Fe II}}/W_{2796}^{\text{Mg II}}$ ([Joshi et al. 2018](#)) as GOTOQ typically fall in this class of Mg II absorbers. In the middle and the bottom panels of Fig-

ure 10, we show the same for the “GOTOQ-Ext” and the “GOTOQ-Noext” sub-samples respectively. Compared to the “GOTOQ-Noext” systems ($A_V = 0.049 \pm 0.001$ and $E(B - V) \sim 0.018$), the “GOTOQ-Ext” ($A_V = 0.070 \pm 0.002$; $E(B - V) \sim 0.025$) systems are slightly more reddened. This trend is consistent with the known correlation between the Mg II equivalent width and $E(B - V)$ ([Budzynski & Hewett 2011](#)).

4.2.2 Average metallicity and ionization parameter of the nebular emission regions

In this section, we use the average nebular emission line luminosities to derive the gas phase metallicity and ionization parameters. To estimate the median emission line luminosities, we first fitted continuum to individual spectrum using the package PYQSOFIT ([Guo et al. 2018](#)). Then, we subtracted each quasar continuum from their respective GOTOQ spectrum and then converted the fluxes to the line luminosities depending on the redshift of the foreground galaxies for the cosmological parameters assumed in this work. Then we performed a simple median stack of these systems. The median emission line luminosities for [O II], [O III] and H β obtained from the stacked spectrum are listed in Table 4. The method used is very much similar to that of [Noterdaeme et al. \(2010b\)](#); [Ménard et al. \(2011\)](#) and [Joshi et al. \(2017\)](#). As we do not incorporate the correction for fiber loss, the quoted average nebular line luminosities are lower limits. However, we proceed with the assumption that this correction factor is nearly the same for the nebular emission lines used. Therefore, fiber effects do not affect the line luminosity ratios that are crucial for deriving the parameters.

Based on the nebular emission line luminosities, we measure the ionization parameter (q) and the gas phase metallicity (Z) of the foreground galaxies using the PYTHON fork ([Mingozi et al. 2020](#)) of the IZI ([Blanc et al. 2015](#), Inferring metallicity and ionization parameter) and assuming the photoionization model of [Levesque et al. \(2010\)](#). The measured values of q and Z are given in Table 6. It is evident that for the full as well as different sub-samples, the average derived metallicities are $12 + \log(\text{O}/\text{H}) \sim 8.3$ (see also the

Table 6. Measurement of gas-phase metallicity, the ionization parameters, and the stellar masses for the different GOTOQ samples based on emission line ratios and the SED fitting.

Sample	Z $12 + \log(O/H)$	q $\log(cm\ s^{-1})$	Mass $\log(M_*/M_\odot)$	SFR M_\odot/yr	Age Gyr
low redshift bin					
All	$8.32^{+0.09}_{-0.11}$	$7.64^{+0.04}_{-0.09}$	$9.76^{+0.10}_{-0.08}$	$2.38^{+0.23}_{-0.26}$	$3.97^{+0.86}_{-0.67}$
GOTOQ-Ext	$8.31^{+0.10}_{-0.06}$	$7.73^{+0.05}_{-0.08}$	-	-	-
GOTOQ-Noext	$8.32^{+0.09}_{-0.08}$	$7.62^{+0.04}_{-0.07}$	-	-	-
mid redshift bin					
All	$8.32^{+0.02}_{-0.04}$	$7.57^{+0.02}_{-0.05}$	$9.46^{+0.14}_{-0.14}$	$1.57^{+0.21}_{-0.24}$	$3.07^{+1.14}_{-0.82}$
GOTOQ-Ext	$8.32^{+0.06}_{-0.04}$	$7.58^{+0.04}_{-0.03}$	-	-	-
GOTOQ-Noext	-	-	-	-	-
high redshift bin					
All	$8.31^{+0.09}_{-0.10}$	$7.69^{+0.06}_{-0.10}$	$9.81^{+0.10}_{-0.08}$	$4.48^{+0.41}_{-0.40}$	$2.59^{+0.54}_{-0.42}$
GOTOQ-Ext	$8.31^{+0.29}_{-0.28}$	$7.70^{+0.12}_{-0.14}$	-	-	-
GOTOQ-Noext	$8.31^{+0.06}_{-0.07}$	$7.67^{+0.05}_{-0.08}$	-	-	-

Table 4 of [Joshi et al. 2017](#)), this is roughly a factor 2 less than the solar metallicity (Z_\odot , $(12 + \log(O/H)) = 8.69$). The q and Z are similar for our GOTOQ-Ext and GOTOQ-Noext sub-samples. We also did not find a clear evolution of these parameters with redshift over the small redshift range considered here.

Note that the average metallicity derived here is less than what is measured in the case of USMgII systems at similar redshifts by [Guha et al. \(2022\)](#). Even in few individual GOTOQs (with clear detections of all the nebular lines) where these measurements are made, the metallicities of GOTOQs are often sub-solar (see figure 8 of [Guha et al. 2022](#)). Based on the known stellar mass-metallicity relationship, this could imply the average stellar mass of the GOTOQs is lower than that of USMgII. If we use the Stellar mass- gas phase metallicity relationship found by [Ma et al. \(2016\)](#) we find the expected median stellar mass (M_*) to be in the range 10^9 to $3 \times 10^9 M_\odot$. Below, we compare this with what we find through the SED fitting exercise.

The q values measured for the different sub-samples of GOTOQs are in the range $7.5 \leq \log q\ (cm\ s^{-1}) \leq 7.7$. These values are slightly higher than the mean q value (i.e $\log q = 7.29 \pm 0.23$) found for extra-galactic H II regions in nearby spiral galaxies ([Blanc et al. 2015](#)). It is known in the literature that metallicity and q are anti-correlated ([Kewley et al. 2019](#)). Thus slightly elevated q values in our sample are expected as the average metallicity is a factor 2 less than solar.

4.2.3 Median spectrum: Nature of galaxies

The median stacked spectrum obtained for the low- z GOTOQ sample is shown in black in the middle panel of Figure 11. In this panel, we also indicate the rest wavelengths of various emission and absorption features expected in the galaxy spectrum using blue vertical dashed lines. In addition to the nebular lines we have detected in individual cases (i.e., [O II], [O III] and H β), we detect H γ and H δ in emission and higher Balmer lines in absorption in the composite spectrum. Note, because of fiber loss, we might have underestimated the emission line fluxes in individual cases and in the composite spectrum. However, as noted above, we assume that the line ratios are not severely affected by fiber loss.

The stacked spectrum shown has contributions from both the background quasars and the foreground galaxies. We assume the average contribution from the background quasars to be a power law and model the median stacked spectrum as a linear combination of the power law and a model galaxy template. For this, we use the model galaxy templates obtained from [Fraix-Burnet et al. \(2021\)](#) who classified the SDSS galaxies in 86 different spectroscopic classes using the k-means clustering algorithm. From these 86 spectroscopic classes, based on the least square minimization, we identify the best fit spectroscopic template. In this exercise, we have avoided the templates that might have contributions from AGN in addition to the stellar and nebular emissions.

In Figure 11, the spectrum shown in red corresponds to the best-fitted galaxy template added to the power law contribution from quasars. The best-fitted galaxy template corresponds to the spectra class ‘B17’ ([Fraix-Burnet et al. 2021](#)), which are basically irregular star-forming galaxies. From the middle panel of Figure 11, it is apparent that most of the Balmer absorption and emission lines present in the stacked GOTOQ spectrum are reproduced by this template. In the top panel, we show a zoomed-in power-law subtracted version of the fit from the middle panel to point out how well the galaxy template used captures the Balmer absorption and emission lines. We notice that Ca II $\lambda\lambda$ 3935, 3970 absorption is much stronger than what has been seen in the template. We believe that considerable Ca II absorption originates from the CGM gas that produces the Mg II absorption along our line of sight. We repeat the same exercise for the three redshift bins and find that among the available star-forming galaxy templates, ‘B17’ best fits the stacked GOTOQ spectrum for all the three redshift bins considered here. Although the ‘B17’ template provides the best least square minimization, it does not very correctly produce the emission line ratios seen in the stacked spectrum. The model spectra of spectral class ‘A30’ ([Fraix-Burnet et al. 2021](#)), which corresponds to the composite spiral galaxies of Hubble type ‘S0’, mimics the emission line ratios for all three redshift bins.

In the bottom panel of Figure 11, We show the best-fitted galaxy template (in blue) scaled by the flux we measured in the stacked images for the low- z GOTOQs (given in Table 4). We fit this best-fitting template (appropriately scaled

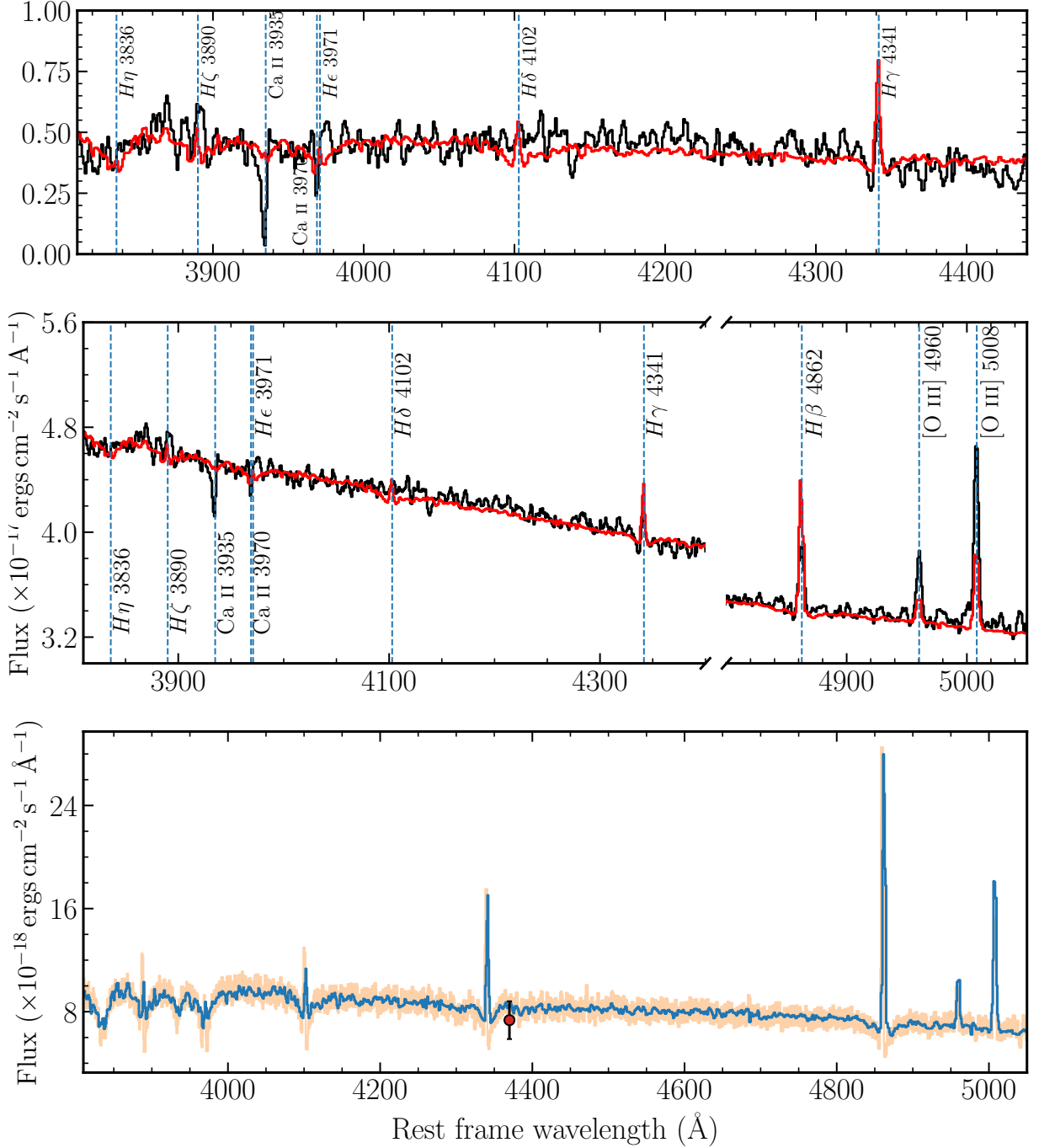


Figure 11. *Middle panel:* The median stacked spectrum of the GOTOQs in the low- z bin (black) and the best fit model (red) to this spectrum (power law + galaxy template) are shown. The blue dashed vertical lines show the expected locations of the prominent emission and absorption lines. *Top panel:* The power-law subtracted stacked GOTOQ spectrum and the best fit model around the region containing Ca II absorption and Balmer lines from the middle panel are shown. *Bottom panel:* The best-fitted galaxy template (blue) appropriately scaled to match the median flux (red point with error bar) seen in the stacked image of the low- z sample. The spectrum shown in orange is the SED fit that recovers all the nebular emissions, galactic absorption, and the stellar continuum features.

to match the average flux measured in stacked images as shown in the bottom panel of Figure 11) using SED fitting techniques (discussed below) to derive parameters of the galaxies.

4.2.4 Estimating Galaxy Parameters

Using the three-band photometric measurements and our stacked spectra, we infer the average galaxy properties by fitting the spectral energy distribution (SED) of the galaxies in each of the redshift bins. For this purpose, we make use of the publicly available SED fitting code-named Bayesian

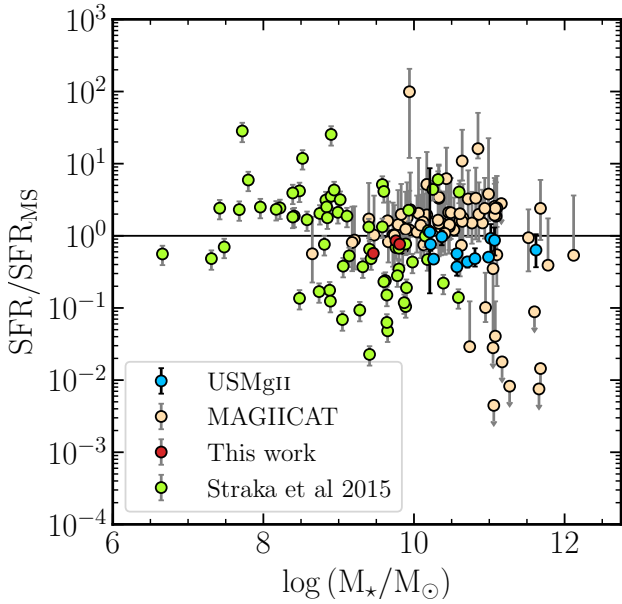


Figure 12. Comparison of the average properties of our GOTOQ host galaxy (red) from the three redshift bins with that of the population of normal Mg II absorbers (light orange, MAGICAT), GOTOQ (Straka et al. 2015, light green), and the USMgII (sky blue) systems. In the x-axis, we plot the stellar mass, and in the y-axis, we show the SFR scaled with respect to the main sequence SFR for the given stellar mass and the galaxy redshift. It is clear that the GOTOQ host galaxies have lower stellar mass but roughly follows the main sequence relations.

Analysis of Galaxies for Physical Inference and Parameter Estimation (Carnall et al. 2018, BAGPIPES). BAGPIPES assumes the stellar population synthesis models by Bruzual & Charlot (2003) and the implementations of the nebular emission lines from Byler et al. (2017). Under the energy balance principle, we assume the Calzetti (1997) dust extinction law, such that dust-absorbed energy is re-radiated in the far infrared. All stellar populations have this effective absorption, while the youngest stars (defined as those with age < 10 Myr) suffer an extra factor of attenuation (η , assumed to be 2.27) to account for dusty birth clouds. We also assume the delayed exponential star formation history. The obtained average stellar masses, the star formation rate, and the age of the GOTOQ in the three redshift bins are given in Table 6. The average stellar masses obtained for three redshift bins range from 9.46 to 9.81 while the SFR ranges from 1.57 to $4.48 M_{\odot} \text{ yr}^{-1}$. The stellar age ranges from 2.59 Gyr to 3.97 Gyr. We note that the stellar mass derived by just fitting the SED to the three photometric points we have from the stacked images is also consistent with this value. Using the spectrum allows us to place additional constraints on age and SFR. For the 53 GOTOQs studied by Straka et al. (2015), the stellar masses ($\log(M_{*}/M_{\odot})$) of the foreground galaxies range from 7.34 to 11.54 (with a median value of 9.05), and SFR ranges from 0.01 to $12 M_{\odot} \text{ yr}^{-1}$ (with a median value of $0.54 M_{\odot} \text{ yr}^{-1}$). Note that these SFR values should be considered as lower limits as they are based on H α luminosity that is affected by fiber size effects.

In Figure 12, we plot the current star formation rate scaled with respect to the main sequence star-formation rate (Speagle et al. 2014) for the same stellar mass and the galaxy

redshift vs. stellar mass for different samples of Mg II host galaxies. For the general population of the Mg II absorbers, we consider objects in the well-known MAGICAT (Nielsen et al. 2013b) sample of the Mg II absorption systems. MAGICAT survey is a compilation of a total of 182 Mg II absorption systems over the redshift ranges of $0.07 \leq z_{\text{abs}} \leq 1.12$ with the host galaxies identified up to a maximum impact parameter of about 200 kpc. To compare against the GOTOQ, however, we only consider the isolated Mg II host galaxies (defined as the only host galaxy lying within a maximum impact parameter of 100 kpc within a maximum velocity separation of 500 km s^{-1} within maximum impact parameters of 60 kpc. Among the 98 isolated Mg II host galaxies present within the impact parameter of 60 kpc in the MAGICAT survey, only 76 galaxies are identified as the photometric sources for which multiband reliable photometric analysis can be performed. For these 76 Mg II host galaxies, we have performed the SED fitting exercise using BAGPIPES to estimate the host galaxy properties like the stellar mass and the current star formation rate (SFR). The host galaxy properties of the USMgII host galaxies are taken from Guha et al. (2022) who compiled a sample of USMgII absorption systems accessible to the SALT ($\delta \leq 10^0$) within the redshift range of $0.4 \leq z_{\text{abs}} \leq 0.6$. We also show the results for GOTOQ from Straka et al. (2015). However, note that these points suffer from the aperture correction as SFR is estimated using H α luminosity.

In Figure 12, the points for USMgII, MAGICAT, and the GOTOQ host galaxies are plotted in sky blue, light orange, and light green colors, respectively. The average properties in the three redshift bins for the GOTOQ sample obtained from this work are shown in red. The horizontal line corresponds to the main sequence star formation. Unlike the USMgII host galaxies, which are likely to be the post-starburst galaxies (Guha et al. 2022), the GOTOQ host galaxies are, on average, following the star-forming main sequence. It is also evident the average stellar mass (and SFR) found for the GOTOQs are on the lower side of what has been measured for the MAGICAT galaxies and much lower than what has been measured in the case of USMgII.

5 SUMMARY AND CONCLUSIONS

Frequency of occurrence and redshift evolution of Mg II absorption systems inferred from the spectra of high- z quasars favor the existence of extended CGM around galaxies. Sustaining such a large reservoir of gas over cosmic time requires an equilibrium between outflowing gas from the galaxies and infalling gas into the galaxies. In particular, "down-the-barrel" spectroscopy of high- z galaxies and spectroscopy of close pairs of background quasars and foreground galaxies are important to probe the nature of outflows at the interface between gaseous disk and CGM of galaxies. The host galaxies of GOTOQs and USMgII absorbers provide ideal targets to study quasar galaxy pairs at low impact parameters. Here, we study the nature of host galaxies of 198 GOTOQs in the sample of Joshi et al. (2017) using DESI Legacy Imaging Survey, SDSS spectra, image decomposition, and spectral and image stacking methods. Below, we summarize our findings.

1. We report the measurements of impact parameter (D) and absolute B-band magnitudes (M_B) for 74 systems, where

decomposition of galaxy image from the quasar is possible in the DESI legacy survey images. The measured impact parameters are in the range $5.9 \leq D[kpc] \leq 16.9$. Our data alone does not show the well-known correlation between W_{2796} and D . However, our data combined with the literature data is well-fitted with a log-linear relationship (albeit with a large scatter in W_{2796} for a given D). We measure $W_{2796}(D=0) = 3.44 \pm 0.20 \text{ \AA}$ and a exponential scale length of $21.6^{+2.41}_{-1.97} kpc$ for the Mg II equivalent width profile. We find neither of these parameters to show significant evolution with z over $0.39 \leq z \leq 1.05$. The value of $W_{2796}(D=0)$ obtained here is larger than what has been found by Kacprzak et al. (2013). This could just be due to their fit being weighted by a large number of measurements at large D , and an available handful of measurements at small D not capturing the intrinsic scatter in the W_{2796} .

Joshi et al. (2017) have shown that the distribution of W_{2796} in our sample (see their figure 7 and associated discussions in section 4.1) is statistically closer to what has been seen along ISM+halo sightlines of the Milky Way (MW) than that of absorption from the MW halo. Kacprzak et al. (2013) found the same for absorbers with $D \leq 6 kpc$ in their sample. Joshi et al. (2017) have also shown that the ratio of equivalent widths of Fe II $\lambda 2600$ and Mg II $\lambda 2796$ is systematically larger in our GOTOQs compared to the general population of Mg II absorbers. Our results support the model in which low impact parameter sightlines probe different populations of gas (disk+halo) compared to high impact parameter sightlines that mainly probe the halo gas. This picture is also endorsed by the fact that nearly all the GOTOQs are also either DLAs or sub-DLAs (see Kulkarni et al. 2022). A smooth fit to the full sample using a log-linear fit may appear remarkable in this picture. But we wish to point out that this fit does have a large scatter, and it is important to look at properties other than W_{2796} to probe distinction in the physical conditions of the gas at different radial distance scales from the galaxy. In this regard, measuring impact parameters in the remaining 124 GOTOQs in our sample using high spatial resolution observations will provide much tighter constraints on the W_{2796} vs. D distribution at the low- D range.

2. The observed B-band absolute magnitudes are in the range $-22.34 \leq M_B \leq -18.72$ mag. This corresponds to the rest frame B-band luminosity in the range $0.075 L_B^*$ to $2.07 L_B^*$, L_B^* being the characteristic luminosity as defined in the Schechter function. We find a strong anti-correlation between M_B and D and a moderate correlation between M_B and W_{2796} in our sample, as has been the case for systems in the MAGICAT sample that typically probes larger impact parameters than our sample. These are consistent with brighter galaxies hosting larger CGM gas that produces large Mg II absorption line equivalent width (large velocity spread and the number of clouds), albeit with a large scatter.

3. We performed an image stacking exercise to measure the average properties of host galaxies of all the 198 GOTOQs in our sample. To avoid the effect of evolving physical size for a fixed angular scale over redshift, we divide the sample into three redshift bins. Host galaxies are clearly detected in all three redshift bins and all three photometric bands used in the DESI legacy imaging survey. From the stacked images, we obtain the maximum impact parameter of our sample to be in the range $15 \leq D[kpc] \leq 16.4$ and the average B-band luminosity to be of the $\sim 0.3 L_B^*$. We also performed the image

stacking exercise for the sub-samples where the host galaxies parameters are directly measurable (i.e. ‘‘GOTOQ-Ext’’ sub-sample) and where the host galaxies are not clearly visible (i.e. ‘‘GOTOQ-Noext’’ sub-sample). There is an indication for the impact parameters in the case of the ‘‘GOTOQ-Noext’’ sub-sample being smaller than that of the ‘‘GOTOQ-Ext’’ sub-sample. However, the average M_B values inferred from the two samples are consistent with each other. Therefore, we conclude that the difficulty in detecting host galaxies in the case of the ‘‘GOTOQ-Noext’’ sub-sample is probably related to the impact parameters being less in these cases. The lack of any difference in the distribution of W_{2796} between the two sub-samples is also consistent with the flattening of W_{2796} vs. D distribution with a large scatter at small D .

4. We performed different spectral stacking methods (i.e., median and geometric mean combined spectra) on the SDSS spectra to probe the average equivalent widths of CGM absorption lines, E(B–V), and spectral signatures (nebular emission and stellar absorption) from the host galaxies. The absorption lines of strong transitions of Mg II and Fe II in the GOTOQ sample are found to be stronger than what has been seen in strong Mg II absorbers, Ca II and H I 21-cm absorption selected systems. However, rest equivalent widths of Mg I and weaker transitions of Fe II (such as at 2249 Å and 2260 Å) lines are similar to what has been found in the above-mentioned absorbers. We also find an average $E(B-V) = 0.021 \pm 0.001$ for our sample. This is consistent with what is found for the full Ca II-selected absorbers (Sardane et al. 2015) but less than what is found for the strong Ca II-selected absorbers and H I 21-cm absorbers (Dutta et al. 2017a).

5. In the median stack of continuum-subtracted spectra, we detect nebular emission lines. We use the ISI code of Blanc et al. (2015) to estimate the average metallicity (Z) and ionization parameter (q) in three redshift bins. The inferred average metallicity ($12 + \log(O/H) \sim 8.3$) is less than the solar metallicity and corresponds to a stellar mass of $1 - 3 \times 10^9 M_\odot$ if we use the known stellar mass-metallicity relationship at these redshifts. The q values measured for the different sub-samples are slightly higher than the mean q value (i.e. $\log q \sim 7.29 \pm 0.23$) found for extra-galactic H II regions in nearby spiral galaxies (Blanc et al. 2015). It is known in the literature that the metallicity and q are anti-correlated (Kewley et al. 2019). Thus slightly elevated q values in our sample are expected as the average metallicity is a factor 2 less than solar metallicity.

6. We show that the median stacked spectrum can be well fitted by a QSO contribution approximated by a power-law plus the galaxy template ‘B17’ of Fraix-Burnet et al. (2021). This template roughly follows the transition from emission to absorption in the case of Balmer lines, as observed in our stacked spectrum. This suggests on average GOTOQ host galaxies are irregular star-forming galaxies. We use the best-fitted galaxy template spectrum and magnitudes obtained from the image stacking in three redshift bins to derive the average star formation rate, stellar mass, and age using SED fitting. The average stellar mass inferred for the GOTOQs is typically less than what has been measured in the case of Mg II absorbers in the MAGICAT and USMgII samples. We find that the average SFR inferred is consistent with what is expected for the main sequence based on the inferred average stellar mass.

High spatial resolution imaging of our full sample (either with space observatories or using adaptive optics from ground-based facilities) is important to directly measure the impact parameter and orientation of galaxies for all the GO-TQs in our sample. Such observations will allow us to study the W_{2796} vs. D correlations at $D \leq 10$ kpc values and quantify the effect of galaxy orientation on the absorption profile. High spatial resolution spectroscopic observations will allow us to probe the absorbing gas toward both quasars and galaxies (i.e., down-the-barrel). Such observations, which will become possible with next-generation optical telescopes, will provide important insights into the gas distribution and different feedback processes operating at ≤ 10 kpc to the high- z star-forming galaxies.

6 ACKNOWLEDGEMENT

We thank the anonymous referee, Dr. Jens-Kristian Kroger, Dr. Rajeshwari Dutta, for their comments on the manuscript. This project makes use of the following softwares : NumPy (Harris et al. 2020), SciPy (Virtanen et al. 2020), Matplotlib (Hunter 2007), and AstroPy (Astropy Collaboration et al. 2013, 2018). This paper makes use of SDSS observational data. Funding for the Sloan Digital Sky Survey IV has been provided by the Alfred P. Sloan Foundation, the U.S. Department of Energy Office of Science, and the Participating Institutions. SDSS-IV acknowledges support and resources from the Center for High-Performance Computing at the University of Utah. The SDSS website is www.sdss.org. SDSS-IV is managed by the Astrophysical Research Consortium for the Participating Institutions of the SDSS Collaboration, including the Brazilian Participation Group, the Carnegie Institution for Science, Carnegie Mellon University, Center for Astrophysics | Harvard & Smithsonian, the Chilean Participation Group, the French Participation Group, Instituto de Astrofísica de Canarias, The Johns Hopkins University, Kavli Institute for the Physics and Mathematics of the Universe (IPMU) / University of Tokyo, the Korean Participation Group, Lawrence Berkeley National Laboratory, Leibniz Institut für Astrophysik Potsdam (AIP), Max-Planck-Institut für Astronomie (MPIA Heidelberg), Max-Planck-Institut für Astrophysik (MPA Garching), Max-Planck-Institut für Extraterrestrische Physik (MPE), National Astronomical Observatories of China, New Mexico State University, New York University, University of Notre Dame, Observatório Nacional / MCTI, The Ohio State University, Pennsylvania State University, Shanghai Astronomical Observatory, United Kingdom Participation Group, Universidad Nacional Autónoma de México, University of Arizona, University of Colorado Boulder, University of Oxford, University of Portsmouth, University of Utah, University of Virginia, University of Washington, University of Wisconsin, Vanderbilt University, and Yale University.

The DESI Legacy Imaging Surveys consist of three individual and complementary projects: the Dark Energy Camera Legacy Survey (DECaLS), the Beijing-Arizona Sky Survey (BASS), and the Mayall z -band Legacy Survey (MzLS). DECaLS, BASS, and MzLS together include data obtained, respectively, at the Blanco telescope, Cerro Tololo Inter-American Observatory, NSF's NOIRLab; the Bok telescope, Steward Observatory, University of Arizona; and the May-

all telescope, Kitt Peak National Observatory, NOIRLab. NOIRLab is operated by the Association of Universities for Research in Astronomy (AURA) under a cooperative agreement with the National Science Foundation. Pipeline processing and analyses of the data were supported by NOIRLab and the Lawrence Berkeley National Laboratory (LBNL). Legacy Surveys also uses data products from the Near-Earth Object Wide-field Infrared Survey Explorer (NEOWISE), a project of the Jet Propulsion Laboratory/California Institute of Technology, funded by the National Aeronautics and Space Administration. Legacy Surveys was supported by: the Director, Office of Science, Office of High Energy Physics of the U.S. Department of Energy; the National Energy Research Scientific Computing Center, a DOE Office of Science User Facility; the U.S. National Science Foundation, Division of Astronomical Sciences; the National Astronomical Observatories of China, the Chinese Academy of Sciences and the Chinese National Natural Science Foundation. LBNL is managed by the Regents of the University of California under contract to the U.S. Department of Energy. The complete acknowledgments can be found at <https://www.legacysurvey.org/acknowledgment/>. The Photometric Redshifts for the Legacy Surveys (PRLS) catalog used in this paper was produced thanks to funding from the U.S. Department of Energy Office of Science, Office of High Energy Physics via grant DE-SC0007914.

7 DATA AVAILABILITY

All the spectroscopic and the photometric data used in this work are publicly available from the SDSS² and the DESI Legacy Imaging Surveys respectively³.

REFERENCES

- Astropy Collaboration et al., 2013, *A&A*, **558**, A33
- Astropy Collaboration et al., 2018, *AJ*, **156**, 123
- Blanc G. A., Kewley L., Vogt F. P. A., Dopita M. A., 2015, *ApJ*, **798**, 99
- Bond N. A., Churchill C. W., Charlton J. C., Vogt S. S., 2001, *The Astrophysical Journal*, **562**, 641
- Bordoloi R., Lilly S. J., Kacprzak G. G., Churchill C. W., 2014, *The Astrophysical Journal*, **784**, 108
- Bruzual G., Charlot S., 2003, *Monthly Notices of the Royal Astronomical Society*, **344**, 1000
- Budzynski J. M., Hewett P. C., 2011, *MNRAS*, **416**, 1871
- Byler N., Dalcanton J. J., Conroy C., Johnson B. D., 2017, *ApJ*, **840**, 44
- Calzetti D., 1997, *AJ*, **113**, 162
- Carnall A. C., McLure R. J., Dunlop J. S., Davé R., 2018, *Monthly Notices of the Royal Astronomical Society*, **480**, 4379
- Chen H.-W., Helsby J. E., Gauthier J.-R., Shectman S. A., Thompson I. B., Tinker J. L., 2010, *The Astrophysical Journal*, **714**, 1521
- Dey A., Torrey P., Rubin K. H. R., Zhu G. B., Suresh J., 2015, *Monthly Notices of the Royal Astronomical Society*, **451**, 1806
- Dey A., et al., 2019, *AJ*, **157**, 168
- Dutta R., Srianand R., Gupta N., Momjian E., Noterdaeme P., Petitjean P., Rahmani H., 2017a, *MNRAS*, **465**, 588

² <https://www.sdss.org/>

³ <https://www.legacysurvey.org/>

- Dutta R., Srianand R., Gupta N., Momjian E., Noterdaeme P., Petitjean P., Rahmani H., 2017b, *MNRAS*, **465**, 588
- Dutta R., et al., 2020, *MNRAS*, **499**, 5022
- Dutta R., et al., 2021, *MNRAS*, **508**, 4573
- Erb D. K., 2008, *The Astrophysical Journal*, **674**, 151
- Faber S. M., et al., 2007, *ApJ*, **665**, 265
- Fraix-Burnet D., Bouveyron C., Moulata J., 2021, *A&A*, **649**, A53
- Gauthier J.-R., 2013, *Monthly Notices of the Royal Astronomical Society*, **432**, 1444
- Gordon K. D., Clayton G. C., Misselt K. A., Landolt A. U., Wolff M. J., 2003, *ApJ*, **594**, 279
- Guha L. K., Srianand R., Dutta R., Joshi R., Noterdaeme P., Petitjean P., 2022, *MNRAS*, **513**, 3836
- Guo H., Shen Y., Wang S., 2018, PyQSOFit: Python code to fit the spectrum of quasars, Astrophysics Source Code Library, record ascl:1809.008 (ascl:1809.008)
- Gupta N., Srianand R., Bowen D. V., York D. G., Wadadekar Y., 2010, *MNRAS*, **408**, 849
- Gupta N., Srianand R., Petitjean P., Bergeron J., Noterdaeme P., Muzahid S., 2012, *A&A*, **544**, A21
- Harris C. R., et al., 2020, *Nature*, **585**, 357–362
- Houck J. C., Bregman J. N., 1990, *The Astrophysical Journal*, **352**, 506
- Huang Y.-H., Chen H.-W., Shethman S. A., Johnson S. D., Zahedy F. S., Helsby J. E., Gauthier J.-R., Thompson I. B., 2021, *MNRAS*, **502**, 4743
- Hunter J. D., 2007, *Computing in Science Engineering*, **9**, 90
- Joshi R., Srianand R., Petitjean P., Noterdaeme P., 2017, *Monthly Notices of the Royal Astronomical Society*, **471**, 1910
- Joshi R., Srianand R., Petitjean P., Noterdaeme P., 2018, *MNRAS*, **476**, 210
- Kacprzak G. G., 2017, in Fox A., Davé R., eds, *Astrophysics and Space Science Library Vol. 430, Gas Accretion onto Galaxies*. p. 145 ([arXiv:1612.00451](https://arxiv.org/abs/1612.00451)), doi:10.1007/978-3-319-52512-9_7
- Kacprzak G. G., Cooke J., Churchill C. W., Ryan-Weber E. V., Nielsen N. M., 2013, *The Astrophysical Journal*, **777**, L11
- Karademir G. S., et al., 2022, *MNRAS*, **509**, 5467
- Kennicutt R. C., Evans N. J., 2012, *ARA&A*, **50**, 531
- Kewley L. J., Nicholls D. C., Sutherland R. S., 2019, *ARA&A*, **57**, 511
- Kulkarni V. P., Bowen D. V., Straka L. A., York D. G., Gupta N., Noterdaeme P., Srianand R., 2022, *ApJ*, **929**, 150
- Levesque E. M., Kewley L. J., Larson K. L., 2010, *AJ*, **139**, 712
- Lopez S., et al., 2018, *Nature*, **554**, 493
- Ma X., Hopkins P. F., Faucher-Giguère C.-A., Zolman N., Muratov A. L., Kereš D., Quataert E., 2016, *MNRAS*, **456**, 2140
- Martin C. L., Shapley A. E., Coil A. L., Kornei K. A., Bundy K., Weiner B. J., Noeske K. G., Schiminovich D., 2012, *The Astrophysical Journal*, **760**, 127
- Mingozi M., et al., 2020, *A&A*, **636**, A42
- Mortensen K., Keerthi Vasan G. C., Jones T., Faucher-Giguère C.-A., Sanders R. L., Ellis R. S., Leethochawalit N., Stark D. P., 2021, *ApJ*, **914**, 92
- Ménard B., Wild V., Nestor D., Quider A., Zibetti S., Rao S., Turnshek D., 2011, *Monthly Notices of the Royal Astronomical Society*, **417**, 801
- Nestor D. B., Johnson B. D., Wild V., Ménard B., Turnshek D. A., Rao S., Pettini M., 2011, *Monthly Notices of the Royal Astronomical Society*, **412**, 1559
- Nielsen N. M., Churchill C. W., Kacprzak G. G., Murphy M. T., 2013a, *ApJ*, **776**, 114
- Nielsen N. M., Churchill C. W., Kacprzak G. G., 2013b, *The Astrophysical Journal*, **776**, 115
- Noterdaeme P., Srianand R., Mohan V., 2010a, *Monthly Notices of the Royal Astronomical Society*, **403**, 906
- Noterdaeme P., Petitjean P., Ledoux C., López S., Srianand R., Vergani S. D., 2010b, *A&A*, **523**, A80
- Putnam M. E., Peek J. E. G., Jeong M. R., 2012, *ARA&A*, **50**, 491
- Rao S. M., Belfort-Mihalyi M., Turnshek D. A., Monier E. M., Nestor D. B., Quider A., 2011, *MNRAS*, **416**, 1215
- Rigby J. R., Charlton J. C., Churchill C. W., 2002, *ApJ*, **565**, 743
- Rubin K. H. R., Prochaska J. X., Koo D. C., Phillips A. C., Martin C. L., Winstrom L. O., 2014, *The Astrophysical Journal*, **794**, 156
- Rubin K. H. R., et al., 2022, *ApJ*, **936**, 171
- Samui S., Subramanian K., Srianand R., 2008, *MNRAS*, **385**, 783
- Sardane G. M., Turnshek D. A., Rao S. M., 2015, *MNRAS*, **452**, 3192
- Shapiro P. R., Field G. B., 1976, *The Astrophysical Journal*, **205**, 762
- Speagle J. S., Steinhardt C. L., Capak P. L., Silverman J. D., 2014, *ApJS*, **214**, 15
- Srianand R., 1996, *ApJ*, **462**, 643
- Srianand R., Gupta N., Petitjean P., Noterdaeme P., Saikia D. J., 2008, *MNRAS*, **391**, L69
- Straka L. A., Whichard Z. L., Kulkarni V. P., Bishof M., Bowen D., Khare P., York D. G., 2013, *MNRAS*, **436**, 3200
- Straka L. A., et al., 2015, *Monthly Notices of the Royal Astronomical Society*, **447**, 3856
- Tremonti C. A., Moustakas J., Diamond-Stanic A. a. M., 2007, *The Astrophysical Journal*, **663**, L77
- Tumlinson J., et al., 2011, *Science*, **334**, 948
- Tumlinson J., et al., 2013, *ApJ*, **777**, 59
- Virtanen P., et al., 2020, *Nature Methods*, **17**, 261
- Wild V., Hewett P. C., Pettini M., 2007, *MNRAS*, **374**, 292
- York D. G., et al., 2006, *MNRAS*, **367**, 945
- York D. G., et al., 2012, *MNRAS*, **423**, 3692
- Zhou R., et al., 2021, *MNRAS*, **501**, 3309
- Zhu G., Ménard B., 2013a, *ApJ*, **770**, 130
- Zhu G., Ménard B., 2013b, *ApJ*, **773**, 16

APPENDIX A: GOTOQ WITH PHOTOMETRIC EXTENSIONS

This paper has been typeset from a \LaTeX file prepared by the author.

Table A1. GOTOQ with photometric extensions and their properties. Fluxes and the associated errors are measured in nanomaggies.

GOTOQ	RA	Dec	Plate	Fiber	MJD	z_{qso}	z_{abs}	D (kpc)	flux(nm)	error(nm)	z_{ph}	z_{ph}^{err}
J0009+1107	2.291708	11.121000	6113	0602	56219	2.6470	0.6804	11.2	1.32	0.05	0.557	0.130
J0044+1524	11.114625	15.410889	6198	0086	56211	2.6090	0.7142	7.0	0.45	0.05	0.834	0.500
J0119+0505	19.974708	5.097472	4425	0122	55864	2.2000	0.4485	8.8	0.98	0.05	0.444	0.102
J0122+2736	20.699042	27.615833	6261	0732	56219	2.2950	0.7849	12.4	0.54	0.04	0.722	0.243
J0129-0032	22.317250	-0.536500	4229	0182	55501	1.8370	0.8991	13.5	2.46	0.04	1.069	0.173
J0131-0401	22.887167	-4.027083	7048	0710	56575	2.2700	0.5017	10.7	2.21	0.03	0.395	0.095
J0235+0059	38.874250	0.987861	3744	0952	55209	2.7160	0.9250	11.6	0.28	0.02	0.943	0.204
J0236-0005	39.079083	-0.091417	0408	0237	51821	0.9806	0.6448	8.6	0.73	0.02	0.970	0.204
J0748+1656	117.210792	16.940417	1920	0217	53314	0.9321	0.6651	15.0	1.09	0.07	0.961	0.147
J0753+3603*	118.395458	36.061250	3791	0894	55501	0.5260	0.3994	14.5	1.23	0.05	0.424	0.160
J0807+0945	121.962625	9.765194	4510	0081	55559	2.5900	0.7470	16.3	1.33	0.05	0.568	0.074
J0808+0641	122.036125	6.685750	1756	0184	53080	2.1133	0.4326	9.2	2.08	0.07	0.385	0.120
J0810+3328*	122.562417	33.475056	3757	0175	55508	2.2160	0.4643	17.8	2.84	0.08	0.470	0.076
J0826+5533	126.580000	55.556528	5151	0158	56567	2.3930	0.7986	14.7	0.86	0.10	0.691	0.165
J0839+3853	129.977792	38.898333	3765	0606	55508	1.9630	0.6085	6.5	0.42	0.08	0.960	0.234
J0847+3420	131.969208	34.337667	5186	0632	56337	2.4970	0.7371	13.6	0.81	0.11	0.554	0.157
J0855+1933	133.950750	19.558556	5175	0690	55955	1.9270	0.8849	8.3	1.01	0.13	0.913	0.574
J0858+0556	134.627208	5.935000	1191	0283	52674	1.8524	0.4318	7.0	1.83	0.05	0.378	0.117
J0920+3133	140.142917	31.565361	2961	0082	54550	1.7232	0.8035	9.8	0.36	0.04	0.963	0.264
J0929-0126	142.312583	-1.439167	3781	0978	55243	2.2500	0.6990	13.4	0.59	0.06	0.968	0.214
J0930+0018	142.585833	0.307778	3823	0996	55534	2.4300	0.5928	5.9	0.77	0.06	0.473	0.213
J0930+1139*	142.730833	11.665722	5313	0376	55973	0.7860	0.5524	19.5	4.39	0.07	0.543	0.062
J0935+5205*	143.865083	52.096722	0768	0253	52281	2.5787	0.6717	17.8	0.69	0.11	0.726	0.284
J0951+1116	147.992375	11.279361	5321	0844	55945	2.3420	0.7564	12.7	2.94	0.11	0.656	0.062
J0954+2017	148.536250	20.294639	5785	0052	56269	2.2300	0.5488	5.9	1.40	0.07	0.602	0.150
J0959+4809	149.828042	48.161944	1006	0248	52708	1.2848	0.7745	13.2	1.12	0.10	1.032	0.152
J1000+4438	150.064583	44.646639	0942	0511	52703	1.8778	0.7185	9.8	1.28	0.08	0.815	0.277
J1021+2152	155.413333	21.878917	5872	0916	56027	2.2020	0.7601	9.5	0.37	0.07	0.999	0.307
J1023+1427	155.953208	14.462444	5340	0414	56011	2.3080	0.7142	11.7	0.37	0.06	0.675	0.249
J1031+3158	157.786958	31.974639	6451	0640	56358	2.4930	0.5738	10.8	0.63	0.07	0.473	0.097
J1040+0151	160.185667	1.856139	4734	0108	55646	2.1420	0.4455	11.2	1.77	0.07	0.518	0.082
J1041+3101	160.477000	31.029917	2019	0060	53430	0.8559	0.7858	10.5	1.35	0.08	0.817	0.141
J1042+3226*	160.656417	32.437750	6447	0084	56362	2.3500	0.6946	18.4	5.18	0.09	0.726	0.057
J1056+2432	164.044125	24.539833	6418	0604	56354	1.1400	0.3981	16.9	5.08	0.08	0.414	0.135
J1101+1029	165.106000	10.488500	5361	0510	55973	2.5460	0.8563	12.1	0.47	0.05	0.744	0.357
J1102+3159	165.576000	31.993111	6442	0134	56369	2.5630	0.7168	7.0	0.18	0.06	0.519	0.473
J1117+0759	169.482125	7.992278	5369	0393	56272	2.6350	0.7681	8.4	0.32	0.04	0.568	0.151
J1119+5901	169.849208	59.022278	7108	0291	56686	1.3930	0.5316	12.1	2.59	0.09	0.354	0.099
J1130+1245	172.566250	12.765861	1606	0518	53055	1.5024	0.5330	10.5	1.53	0.07	0.430	0.112
J1131+2021	172.784792	20.364194	2502	0371	54180	1.7682	0.5631	7.0	4.10	0.08	0.404	0.234
J1159+3935	179.861458	39.585167	2027	0570	53433	1.6658	0.4921	11.4	3.02	0.09	0.450	0.176
J1215+6135	183.908333	61.590306	6972	0896	56426	2.3150	0.6622	7.4	0.60	0.07	0.823	0.200
J1218+0309	184.658750	3.150028	4750	0774	55630	2.2510	0.5222	11.4	2.57	0.07	0.445	0.063
J1219+6707	184.926667	67.128611	6975	0904	56720	2.4790	0.8029	11.8	0.51	0.08	0.953	0.246
J1230+3652	187.528458	36.874556	3965	0070	55302	2.1200	0.8109	9.7	0.80	0.08	0.952	0.197
J1235+0304	188.809833	3.071306	4754	0592	55649	2.1950	0.5313	13.0	4.04	0.06	0.485	0.054
J1243+5203*	190.881917	52.059750	6674	0926	56416	2.1730	0.7748	20.0	0.33	0.06	0.916	0.246
J1253+4532	193.266292	45.538694	7417	0274	56753	1.3320	0.4424	5.9	1.72	0.08	0.781	0.229
J1253+1758	193.412917	17.975556	2601	0625	54144	0.5042	0.4008	8.5	9.28	0.28	0.494	0.132
J1312+4006	198.181667	40.108583	4706	0156	55705	2.4060	0.7293	8.9	0.23	0.09	0.844	0.165
J1314+0330	198.725833	3.511750	4760	0096	55656	2.7000	0.7792	13.5	0.43	0.07	0.953	0.360
J1346+1236	206.606542	12.604028	1701	0401	53142	1.5233	0.7120	8.0	1.81	0.09	0.704	0.179
J1354+3217*	208.623625	32.285806	3861	0314	55274	0.6830	0.6398	21.8	3.81	0.07	0.523	0.180
J1354+0756	208.690500	7.943778	1806	0043	53559	1.3235	0.7126	14.2	1.74	0.07	0.838	0.116
J1356+0601	209.142333	6.026000	1805	0013	53875	1.3929	0.6292	11.2	1.96	0.05	0.613	0.091
J1416+2214*	214.017167	22.235917	2786	0440	54540	1.1180	0.6995	21.1	4.63	0.08	0.650	0.079
J1417+4730	214.490583	47.502500	6751	0824	56368	1.2410	0.9111	13.0	0.58	0.10	0.920	0.252
J1422+3222	215.608875	32.372528	1840	0202	53472	1.6295	0.5413	11.3	2.44	0.08	0.486	0.094
J1430+5420	217.565125	54.338361	6710	0262	56416	2.7870	1.0582	10.0	0.21	0.07	0.988	0.239
J1435+4740	218.793000	47.682944	1673	0023	53462	0.7844	0.4407	11.3	2.12	0.09	0.443	0.192
J1438+3522	219.501958	35.369000	3865	0702	55272	2.0530	0.7869	11.7	0.39	0.09	0.952	0.206
J1442+6009*	220.630208	60.165083	0607	0037	52368	2.0399	0.7987	21.8	3.48	0.13	0.757	0.126

Table A1. Continued

GOTOQ	RA	Dec	Plate	Fiber	MJD	z_{qso}	z_{abs}	D (kpc)	flux(nm)	error(nm)	z_{ph}	z_{ph}^{err}
J1449+2136	222.490083	21.609139	5905	0696	56065	2.6640	0.7977	8.5	0.76	0.07	0.634	0.717
J1454+4424	223.717667	44.402528	6046	0933	56096	2.3960	0.6630	10.8	1.00	0.11	0.621	0.249
J1502+1806	225.567375	18.115944	3957	0494	55664	1.1110	0.5442	10.9	2.80	0.08	0.474	0.109
J1509+2630	227.368750	26.500778	3872	0246	55382	2.9370	0.7790	12.7	0.62	0.05	0.821	0.143
J1509+1252	227.400375	12.879139	2752	0234	54533	1.9031	0.5405	6.8	1.55	0.06	0.444	0.151
J1518+5815	229.741583	58.257639	0612	0562	52079	1.7390	0.6470	12.2	3.65	0.11	0.458	0.203
J1525+2647	231.260958	26.791861	3959	0466	55679	2.2420	0.9126	13.9	0.63	0.09	0.698	0.343
J1530+4152	232.515208	41.874528	6049	0166	56091	2.3910	0.8468	12.2	0.86	0.06	1.127	0.228
J1634+4849	248.699500	48.829139	6318	0555	56186	2.4960	0.7477	14.5	0.32	0.06	0.730	0.200
J1643+1729	250.868500	17.498722	4062	0130	55383	2.1920	0.5442	9.5	0.89	0.04	0.590	0.299
J1646+2733*	251.678708	27.560889	1690	0439	53475	1.6289	0.7985	17.5	0.71	0.10	0.833	0.258
J1656+4146	254.133917	41.771472	6037	0980	56074	2.1630	0.6622	12.2	2.72	0.13	0.906	0.348
J1657+2045	254.353417	20.766528	1425	0358	52913	1.4585	0.6254	10.8	1.38	0.14	0.416	0.434
J1658+2940	254.742708	29.682083	5013	0664	55723	2.5770	0.8096	7.8	0.27	0.05	1.026	0.543
J2147+1048	326.874958	10.808556	0733	0288	52207	2.1097	0.6990	12.0	0.78	0.09	0.668	0.146
J2150+0225	327.746208	2.432556	5146	0878	55831	2.3780	0.5682	6.9	0.45	0.04	0.919	0.194
J2219+0239	334.960417	2.664750	4319	0286	55507	2.5280	0.7203	10.4	0.56	0.04	0.548	0.162
J2244-0215	341.021208	-2.263306	4363	0778	55537	2.5740	0.9243	16.3	1.22	0.05	1.059	0.097
J2253+2117	343.360667	21.290861	6120	0966	56206	2.4580	0.6994	6.8	0.76	0.08	0.864	0.960
J2324+2427	351.025042	24.464472	6304	0456	56570	2.2780	0.8923	8.7	0.12	0.05	0.961	0.338
J2339+1540	354.916792	15.668278	6138	0488	56598	2.3680	0.7042	11.7	0.48	0.05	0.575	0.185
J2342+0101	355.739583	1.022556	4213	0912	55449	2.4530	0.6768	9.5	0.66	0.02	0.437	0.358